


Review

# A Review on Impacting Parameters for Photocatalytic Degradation of Organic Effluents by Ferrites and Their Nanocomposites

Gurpinder Singh <sup>1</sup>, Manpreet Kaur Ubhi <sup>1</sup>, Kiran Jeet <sup>2</sup>, Chetan Singla <sup>3</sup> and Manpreet Kaur <sup>1,\*</sup> 

<sup>1</sup> Department of Chemistry, Punjab Agricultural University, Ludhiana 141001, Punjab, India; gurpinder-2150001@pau.edu (G.S.); manpreet-cm@pau.edu (M.K.U.)

<sup>2</sup> Department of Soil Science, Punjab Agricultural University, Ludhiana 141001, Punjab, India; kiranjeet@pau.edu

<sup>3</sup> Department of Soil and Water Engineering, Punjab Agricultural University, Ludhiana 141001, Punjab, India; chetan\_singla@pau.edu

\* Correspondence: manpreetchem@pau.edu

**Abstract:** Traditional wastewater treatment methods, such as reverse osmosis, adsorption, desalination, and others, are outweighed by the photocatalytic degradation of organic pollutants. Ferrites are prominent photocatalysts due to their tunable band gaps, surface areas, and magnetic properties, which render photodegradation economical. Ferrites and their nanocomposites have been reported as promising visible light active photocatalysts. The photocatalytic system is heavily reliant on a number of factors that influence the photodegradation of organic effluents. This review demonstrates various parameters such as substrate concentration, pH of solution, photocatalyst quantity, photocatalyst surface area, metal and non-metal ion doping, light intensity, irradiation time, quenchers, etc. affecting the photocatalytic degradation of organic effluents by ferrite nanoparticles and their nanocomposites in detail. The photodegradation efficiency of the ferrite nanoparticles alters with the change in the value of pH of the solution, which further depends upon the nature of the pollutant used. A dose of the substrate and the photocatalyst must be optimized so as to attain better photodegradation efficiency. Photocatalysts with different surface areas change the amount of active sites, which in turn affects the degradation of pollutant and render it a crucial factor. In addition, the mechanism of the action of photocatalysis is elaborated in this review. Future research perspectives for the advancement of ferrites and their nanocomposites are deliberated in order to improve their use as photocatalysts.

**Keywords:** ferrites; nanocomposites; parameters; photodegradation; photocatalyst; mechanism



**Citation:** Singh, G.; Ubhi, M.K.; Jeet, K.; Singla, C.; Kaur, M. A Review on Impacting Parameters for Photocatalytic Degradation of Organic Effluents by Ferrites and Their Nanocomposites. *Processes* **2023**, *11*, 1727. <https://doi.org/10.3390/pr11061727>

Academic Editor: Chiing-Chang Chen

Received: 30 April 2023

Revised: 21 May 2023

Accepted: 28 May 2023

Published: 5 June 2023



**Copyright:** © 2023 by the authors. Licensee MDPI, Basel, Switzerland. This article is an open access article distributed under the terms and conditions of the Creative Commons Attribution (CC BY) license (<https://creativecommons.org/licenses/by/4.0/>).

## 1. Introduction

Organic pollutants in water sources have increased across the world due to the continuous growth of global industry and population. Nearby ecosystems are being poisoned by the toxic and carcinogenic effluents from the pharmaceutical, agricultural, and textile industries, for example [1,2]. These effluents greatly affect groundwater quality, aquatic life, the environment, and human health [3–7]. There are numerous techniques for water treatment, including electro dialysis, electrochemical methods, adsorption, coagulation, bioremediation, and ultrafiltration [8–17]. However, these methods have limitations to the effective purification of wastewaters and investments [18,19].

Advanced oxidation processes (AOPs) are quite effective for wastewater remediation. Reducing the concentration of harmful compounds in wastewater is the primary goal of AOPs before its discharge. To generate high-potential chemical oxidants on-site, ozone (O<sub>3</sub>), UV/visible light, hydrogen peroxide (H<sub>2</sub>O<sub>2</sub>), and Fenton's reagent (Fe(II)/H<sub>2</sub>O<sub>2</sub>) can be used [20]. Photocatalysis is one of the renowned AOPs because photocatalysts can utilize UV/visible or solar energy to degrade pollutants, making photocatalysis economically feasible [21,22]. Photocatalysis is a process whereby a catalyst initiates or stimulates a chemical

reaction using light. This mechanism is referred to as a “photocatalytic reaction” [23,24]. For treating wastewater-containing organic pollutants and dyes, heterogeneous photocatalysis using AOPs is an excellent option because it uses renewable solar energy. Therefore, it is strongly recommended to eliminate organic pollutants and colours [25]. Various reactive species, such as hydroxyl radicals ( $\text{HO}\cdot$ ), superoxide anion ( $\text{O}_2^-$ ), holes ( $\text{h}^+$ ), and singlet oxygen ( $\text{O}_2^1$ ), degrade contaminants adsorbed on the surface of a photocatalyst [26]. Apart from these oxidants, other solution parameters such as the pH of the solution [27], photocatalyst quantity [28], photocatalyst surface area [29], metal and non-metal ion doping [30], light exposure, irradiation time [31], and quenchers [28] also influence the photodegradation of organic pollutants.

Ferrites and their composites—because of their effective adsorption efficiency, excellent visible light catalytic activity, and outstanding Fenton reaction potential—have been regarded as promising materials for the removal of contaminants such as heavy metal/metalloids and organics [32]. Due to the decrease in particle size due to nanoscale confinement and surface effects, the magnetic properties of ferrite nanoparticles display peculiar characteristics that differ from those of bulk equivalent materials [33]. The advantages of magnetic ferrite nanoparticles include their affordability and excellent physical and chemical stability [34]. The magnetic, electric, and optical properties of the matter are affected by the behaviour of the ferrites in the nanoscale range, which is dominated by the quantum effect [35].

As of April 2023, search results on the Science Direct database for the phrase “photocatalytic activity of ferrite” in the titles of publications, keywords, and abstracts of the reviews are displayed in Figure 1. The publications on pure, doped, and composite (binary, ternary, and quaternary)  $\text{MFe}_2\text{O}_4$  are included in the search results. There was a sizable rise in the number of publications between 2015 and 2023. Due to their magnetic properties, simplicity in synthesis, availability of precursors, and biocompatibility, ferrites have received extensive research interest in the field of the photocatalytic degradation of pollutants. The impact of various parameters on the photodegradation of organic pollutants using ferrite and their nanocomposites as photocatalysts, however, is not discussed in any of the reviews. Focusing on these issues, this review provides a thorough discussion of each parameter with regard to the photodegradation of the reported organic pollutants, a brief overview of the synthesis of ferrites and their nanocomposites, and a discussion of the photodegradation mechanism of organic pollutants. Finally, conclusions are drawn and the future research areas that still require attention are listed.

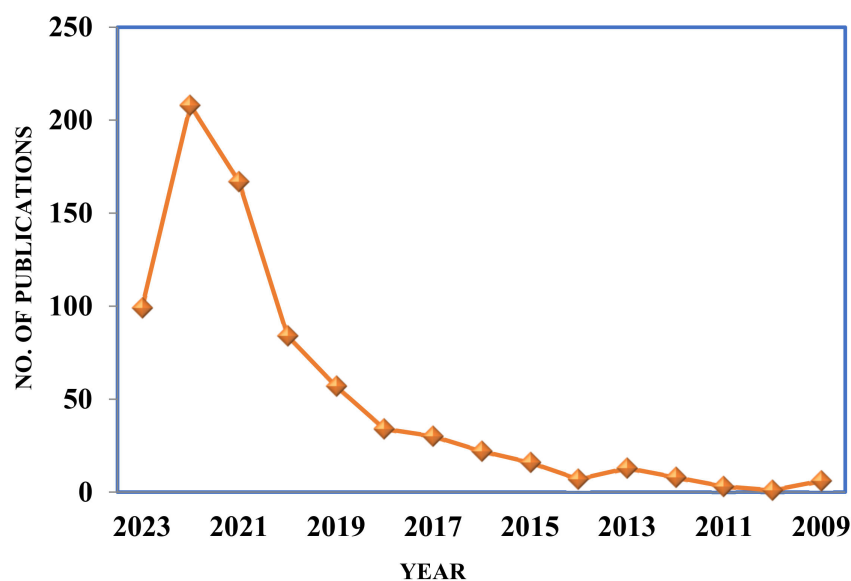


**Figure 1.** Number of publications vs. year. Results obtained from Science Direct database (as of April 2023). Keywords: Photocatalytic activity of ferrite.

## 2. Structure of Ferrites

Ferrites are considered prominent photocatalysts because of their tunable band gaps, stability, distinctive magnetic properties, and low cost of production. In general, the chemical formula of ferrites is  $AB_2O_4$ . The tetrahedral (A) and octahedral (B) sites are occupied by metal cations, and the arrangement of the oxygen anions is cubic closed packing, as shown in Figure 2. This structure can provide different combinations of metal cations due to the balanced negative charges of oxygen anions. When all the A sites are occupied by divalent metal cations and the B sites are occupied by iron (III) cations, the structure that is obtained is called a normal spinel structure, having the formula  $Me^A[Fe_2]^B O_4$ . Inverse spinel ferrites are structures in which an equal number of iron (III) ions occupy both the sites and all the B sites are occupied by divalent metal ions and have the formula  $Fe^A[MeFe]^B O_4$ . Some metal cations strongly prefer a particular site, such as Zn for the A site. Thus,  $ZnFe_2O_4$  is a normal spinel [36–38].

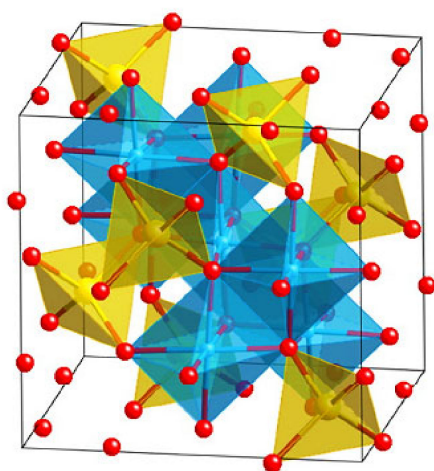


**Figure 2.** Structure of spinel ferrite showing tetrahedral (yellow), octahedral (blue) and oxygen (red) arrangement. Adapted with permission [39]; copyright (2019), Elsevier.

The perfect structure of the mixed ferrite crystals mentioned above, however, are affected by variations in the synthesis conditions, and instead have an empirical formula of  $[M_{1-x}Fe_x]^A[M_xFe_{2-x}]^B O_4$  ( $0 \leq x \leq 1$ ). The addition of a third metal creates ternary [38], with complexity in the arrangement of the metal ions. Ferrites are found to have different electrical, optical, and magnetic properties, as well as different activities in some catalytic reactions, depending on the composition and arrangement of the metal ions [36].

## 3. Methods of Synthesis of Ferrites and Their Nanocomposites

There are many different chemical and physical processes used for the synthesis of ferrite nanoparticles. Chemical-based techniques have been used to synthesise  $Fe_2O_3$  nanoparticles, including reverse micelles [40], co-precipitation [41], sonochemical reactions [42], thermal decomposition [43], sol-gel synthesis [44], hydrothermal [45], and micro-emulsion technology [46].

Ball milling is a mechanical method for solid-state synthesis and is frequently used to grind powders into extremely tiny particles. Being a cost-effective and eco-friendly approach, it is mostly used in industries for large-scale production. However, the size and shape of ferrite nanoparticles are non-uniform. Regulation of the preparative parameters is required, including concentration, pH, type of complexing agent, temperature, etc. Ferrites are typically produced at a temperature of several hundred degrees. At higher temperatures, it is challenging to deposit film ferrites of a consistent quality. In addition, due to the release of poisonous gases during deposition, high-temperature processes are more susceptible to environmental pollution. Oxidation of metallic substrates and corrosion are prevented using low temperature deposition techniques. Table 1 represents the advantages and

disadvantages of various physical and chemical methods used in the synthesis of ferrites and their nanocomposites.

**Table 1.** Advantages and disadvantages of various methods used in the synthesis of ferrites and their nanocomposites.

Type	Methods	Advantages	Disadvantages
Physical	Ball Milling	<ul style="list-style-type: none"> <li>• Bulk synthesis</li> <li>• Rotation speed can affect the particle size</li> <li>• Structural and chemical changes depends on mechanical energy</li> </ul>	<ul style="list-style-type: none"> <li>• Irregular shape and size</li> <li>• Production of contaminants can occur</li> <li>• Disturbance in the lattice structure</li> </ul>
	Sol-gel	<ul style="list-style-type: none"> <li>• Processing temperature is low</li> <li>• Porosity and homogeneity</li> </ul>	<ul style="list-style-type: none"> <li>• Yield of the particles is low</li> <li>• Gases are produced in large amount</li> </ul>
	Co-precipitation	<ul style="list-style-type: none"> <li>• Economic</li> <li>• Low processing temperature</li> </ul>	<ul style="list-style-type: none"> <li>• irregularity in particle shape and size</li> </ul>
Chemical	Combustion	<ul style="list-style-type: none"> <li>• Processing period is low</li> <li>• High yield with purity</li> </ul>	<ul style="list-style-type: none"> <li>• Production of large amount of gases</li> </ul>
	Micro emulsion	<ul style="list-style-type: none"> <li>• Easy processing</li> <li>• Controllable and uniform particle size and homogeneity</li> </ul>	<ul style="list-style-type: none"> <li>• Particle yield is low</li> <li>• liquids are required in large amounts</li> </ul>
	Microwave and Hydrothermal	<ul style="list-style-type: none"> <li>• Yield is high with low processing period</li> </ul>	<ul style="list-style-type: none"> <li>• Costly equipment</li> <li>• Irregularity in particle shape and size</li> </ul>

Among various chemical methods used in the synthesis of ferrites, different methods have their own advantages and disadvantages. For example, the solvothermal method can be used to control the particle size of the synthesized material [47,48]. The sol-gel method is one of the best methods as it yields ferrite with more surface area of the nanoparticles, which is useful for the degradation of pollutants [49–52].

However, due to their magnetic nature and strong magnetic dipole interactions, magnetic NPs are particularly susceptible to agglomeration [53]. The agglomeration observed in these NPs also restricts their use in various applications [53–59]. To overcome these problems, different techniques have been proposed, such as doping and the fabrication of composites using wet chemical methods (hydrothermal, solvothermal), sol-gel, co-precipitation, combustion, and ultrasonication methods. Various ferrites which have been synthesized using these methods and their use as photocatalysts in the degradation of various pollutants is discussed in Table 2.

Hollow microspheres of Ce<sup>3+</sup>-doped NiCo-ferrites were synthesized using a carbon sphere as a template in a template-based deposition and surface reaction method [60]. The hydrothermal method showed the particle size of carbon sphere as 0.5 μm, while the template-based method showed the particle size of Ni<sub>0.5</sub>Co<sub>0.5</sub>Fe<sub>2</sub>O<sub>4</sub> as 300 nm. Graphene-based CuCe<sub>0.2</sub>Fe<sub>1.8</sub>O<sub>4</sub> nanocomposites were synthesized using the hydrothermal method [61,62]. Furthermore, on examining the morphology, thermal stability, and crystal structure of CuFe<sub>2</sub>O<sub>4</sub>, CuCe<sub>0.2</sub>Fe<sub>1.8</sub>O<sub>4</sub> ferrite NPs, and graphene-based CuCe<sub>0.2</sub>Fe<sub>1.8</sub>O<sub>4</sub>, the graphene was found to have distinct effects on the crystallite size, surface morphology, lattice strain, and thermal stability of the CuCe<sub>0.2</sub>Fe<sub>1.8</sub>O<sub>4</sub> ferrite NPs.

Nitrogen-doped 3D magnetic graphene gels were synthesized through one-pot hydrothermal synthesis, and it was found that the reduction in GO, N doping process, and generation of Fe<sub>3</sub>O<sub>4</sub> particles occur simultaneously and are accompanied by 3D self-assembly [63]. Nitrogen-doped magnetic graphene gels were considered organized frameworks of graphene sheets with a uniform dispersion of the Fe<sub>3</sub>O<sub>4</sub> NPs. The wet-chemical method is a synthetic route that deals with the chemical reactions in the solution phase using precursors at proper experimental conditions. The spinel ferrites were prepared through a chemical reaction between aqueous solutions of metal nitrates, ferric nitrates, and oxalyl dihydrazide [64].

**Table 2.** Photocatalytic activity of various ferrite NPs.

S.No.	Compound	Method	Size (nm)	Band Gap (ev)	Surface Area	Pollutant	Catalyst Amount (mg)	Degradation %ge	Ref
1.	ZnFe <sub>2</sub> O <sub>4</sub>	Solvothermal	77	1.65	51.81	RhB	80	100	[65]
		Microwave	40	1.9	6.0	MB	60	32	[66]
		Sol-gel	34.8	1.6	-	OI	400	36.8	[67,68]
2.	MnFe <sub>2</sub> O <sub>4</sub>	Microwave	39	1.56	-	IC	50	94	[69]
3.	CaFe <sub>2</sub> O <sub>4</sub>	Solution combustion	100	1.82	79.3	MB	50	100	[70]
4.	MgFe <sub>2</sub> O <sub>4</sub>	Solid state	-	2	5	MB	50	90	[71]
5.	CuFe <sub>2</sub> O <sub>4</sub>	Co-precipitation	26	1.92	-	4-CP	10	62	[72]
		Solution combustion	8	1.9	-	MG	40	82	[73]
6.	NiFe <sub>2</sub> O <sub>4</sub>	Solution combustion	14	2	-	MG	40	94.5	[73]
		Co-precipitation	29	1.78	13.48	MO	100	83.2	[74]
7.	BaFe <sub>2</sub> O <sub>4</sub>	Sol-gel	-	-	-	BY BV MB AO	10,000	100	[75]
8.	CoFe <sub>2</sub> O <sub>4</sub>	Precipitation	17	3.05	-	MO	100	77	[76]
		Solvothermal	40	2.33	-	MB	50	93	[77]
		Sol-gel	40	1.15	-	RhB	50	78	[78]
9.	CdFe <sub>2</sub> O <sub>4</sub>	Pyrolysis	-	2.06	15.27	CS	30	55.5	[79]
10.	SrFe <sub>2</sub> O <sub>4</sub>	Sol-gel	-	1.75	-	RhB	20	89.3	[80]

RhB—Rhodamine B, MB—Methylene blue, OI—Orange I, IC—Indigo Carmine, 4-CP—4-Chlorophenol, MG—Malachite green, MO—Methyl orange, BY—Basic Yellow, BV—Basic Violet, AO—Acid Orange, CS—Ceftiofur sodium.

In the ultrasonication method, the sound energy is applied to agitate the particles in the solution, which causes physical and chemical transformations for the preparation of nanocomposites [81]. Various studies have demonstrated that this approach is the simplest way to synthesize ferrite-based nanocomposites due to its low-cost and use of distilled water rather than other solvents. The nanocomposite of the carbon quantum dots with trimetallic strontium–titanium ferrite synthesized via an ultrasonication approach possesses a high-specific surface area (101.3 m<sup>2</sup>g<sup>-1</sup>) and a low band gap coupled with fluorescence-quenching, which facilitated the transfer of the photo-induced charge carriers. This feature is very useful for the photodegradation of nitroaromatics [82]. Hierarchical nanoflowers of MgFe<sub>2</sub>O<sub>4</sub>, bentonite and boron, phosphorous co-doped graphene oxide synthesized using the ultrasonication method showed that chiffon-like co-doped graphene oxide nanosheets were wrapped on the MgFe<sub>2</sub>O<sub>4</sub>-bentonite surface, resulting in a porous flower-like morphology. The excellent conductivity of the co-doped nanosheets allowed for

a quick charge carrier transport, which aided in the separation of those carriers during the photocatalytic reaction [83]. Cationic surfactant cetyltrimethyl ammonium bromide was chosen to coat the  $\text{MgFe}_2\text{O}_4$  because its negatively charged surface can interact with the surfactant during ultrasonication [84]. Similarly, the nanocomposite of calcium ferrite with nitrogen-doped graphene oxide ( $\text{CaFe}_2\text{O}_4$ -NGO) with magnetic properties was synthesized using this approach has been effectively used for the degradation of p-nitrophenol [85].

Apart from the ultrasonication method, the sol-gel approach was also used in the synthesis of ferrite-based nanocomposites, and additional material was added during the synthesis of ferrite.  $\text{MgFe}_2\text{O}_4$ -bentonite nanocomposites were synthesized in different *w/w* ratios using this method for the degradation of the p-nitrophenol [86]. The optical band gap of the  $\text{MgFe}_2\text{O}_4$  NPs is 2.58 eV, and this decreases to 2.26 eV with increasing bentonite content in nanocomposites due to the presence of Fermi levels. A similar nanocomposite was synthesized for the degradation of martius yellow. It was found that this nanocomposite showed better degradation for malathion as compared to the p-nitrophenol and martius yellow [87]. This may be due to the resonance stabilization of the structure of the martius yellow [86,88].

Cobalt ferrite/reduced GO nanocomposites were prepared using the membrane-solvothermal method [89]. Scanning electron micrographs of nanocomposite showed the presence of most of the rod-shaped  $\text{CoFe}_2\text{O}_4$  scattered beside the graphene, and only a few  $\text{CoFe}_2\text{O}_4$  nanorods successfully loaded on the graphene. GO-supported ferrite ( $\text{MFe}_2\text{O}_4$ ,  $\text{M} = \text{Fe}, \text{Co}$  and  $\text{Ni}$ ) nanocomposites were prepared using the solvothermal method [90]. The uniform size (20–30 nm) of  $\text{MFe}_2\text{O}_4$  microspheres was seen in the transmission electron micrograph. Vibrational sample magnetometry studies revealed a superparamagnetic behavior of all the nanocomposites with  $M_s$  values between 41 and 43  $\text{emu g}^{-1}$  at room temperature. The removal of the dye pollution was found to be useful with the help of the nanocomposites.

The co-precipitation method is widely used as a liquid phase method in the synthesis of ferrite-based nanocomposites. The co-precipitation and hydrothermal methods were used in the synthesis of core-shell  $\text{ZnFe}_2\text{O}_4/\text{ZnS}$  composites [91]. A characterization of the synthesized composite showed the presence of a layer of ZnS clusters on the surface of the  $\text{ZnFe}_2\text{O}_4$  NPs. The band gap energy was observed to be 2.2 eV, showing the possibility of its application as a photocatalyst under visible light irradiation. The relative energy band positions in the  $\text{ZnFe}_2\text{O}_4$  and ZnS were considered a main advantage for the improved separation of electron-hole pairs. Moreover, the easy magnetic collection of the composite materials was due to the sufficient magnetization of the  $\text{ZnFe}_2\text{O}_4$  core. Thus, the different methods induce different properties in the ferrite-based nanocomposites, and each property has its own advantage for the photocatalytic degradation of organic pollutants.

#### 4. Impacting Parameters for Photocatalytic Activity of Ferrites and Their Nanocomposites

The photocatalytic activity of ferrite NPs and their nanocomposites is reliant on various parameters, such as the substrate concentration, pH of the solution, photocatalyst quantity, surface area of the photocatalyst, metal and non-metal ion doping, light intensity, irradiation time, quenchers, etc. The impact of each parameter on the photodegradation of organic effluents is discussed in detail in the subsequent subsections.

##### 4.1. Effect of pH

Solution pH is an important variable in wastewater treatment as it influences the photocatalytic degradation of organic compounds. The pH of heterogeneous catalysts changes the surface charge, and, as a result, the photocatalytic activity of the catalyst changes [92,93].

The surface charge of the catalyst plays a vital role for the photodegradation of anionic dyes, which was determined using spinel  $\text{Ni}_x\text{Zn}_{1-x}\text{Fe}_2\text{O}_4$  ( $x = 0.0$  to  $1.0$ ) NPs [29]. The maximum degradation was achieved at pH 3, due to the electrostatic desirability among

the anionic dye and the positively charged surface. At basic pH values, the surface of the catalyst became negatively charged, which caused an electrostatic repulsion between the anionic dye and catalyst, thus retarding the degradation of the dyes (Figure 3a). Similar observations were recorded during the photocatalysis of the methylene blue dye using bismuth ferrite ( $\text{BiFeO}_3$ ) NPs, where the dye was completely degraded under visible light irradiation for 80 min [94]. Further, it was reported that sunlight and the presence of a photocatalyst are essential for the dye degradation process. Dye degradation was found to be 53% under dark conditions with the presence of only a catalyst. The dye removal efficiency was negligible in the absence of a catalyst and light. After irradiation under visible light with neutral and acidic pH conditions, no decrease in the concentration of dye was observed. This means that the excitation of dye molecules by photon and then the dispersion of their excitation energy had no role in the decolorization of the dye. However, at a basic pH, the rate of photolysis was high due to the generation of hydroxyl radicals through the generation of hydroxyl ions which degraded the methylene blue dye. This study was supported using an electron spin resonance spectroscopy [95]. The coating of the titania–silica ( $\text{TiO}_2\text{--SiO}_2$ ) on the cobalt ferrite ( $\text{CoFe}_2\text{O}_4$ ) NPs changes the properties on the photocatalyst surface. The  $\text{SiO}_2$  layer between the  $\text{CoFe}_2\text{O}_4$  and  $\text{TiO}_2$  may prevent the charge injection from the semiconductor  $\text{TiO}_2$  to the magnetic  $\text{CoFe}_2\text{O}_4$ , which in turn led to the increase in photocatalytic activity towards the methylene blue dye. Under the acidic conditions, the charge on the  $\text{TiO}_2$  surface was positive, which provided electrostatic interactions for anionic dye molecules [96,97]. The removal of the congo red using  $\text{Ni}_{0.6}\text{Co}_{0.4}\text{Fe}_2\text{O}_4$  was found to be at a maximum for pH 3 (40.28%) and decreased gradually up to pH 10 (15.45%), which was supported by the isoelectric point value of the dye [98].

The Ag/AgBr/ $\text{NiFe}_2\text{O}_4$  plasmonic photocatalyst exhibited a superior photocatalytic performance in the photodecomposition of the cationic Rhodamine B dye under visible light irradiation. The zero-point charge ( $\text{pH}_{\text{zpc}}$ ) of the catalyst was about 5.2. Thus, the composite was negatively charged above that pH and provided electrostatic attractions for the cationic dye molecules [99]. The  $\text{Mn}_{0.5}\text{Zn}_{0.125}\text{Mg}_{0.375}\text{Fe}_2\text{O}_4$  NPs were stabilized at a basic pH, having negative zeta potential ( $-75.14$  eV), which was very important for the photocatalytic degradation of the cationic Rhodamine B dye, as shown in Figure 3b [100]. The ciprofloxacin and remazol deep red dye were degraded using  $\text{MRu}_x\text{Fe}_{2-x}\text{O}_4$  ( $M = \text{Ni}, \text{Cu}$ ) [101]. The dye degradation efficiency was observed to be 93% after 60 min at pH 2.5, which decreased at higher pH levels. In addition,  $\text{H}_2\text{O}_2$  was used to degrade the ciprofloxacin without changing the pH of the pure solution. The ciprofloxacin degraded to its greatest extent over a 120-min period at pH 2.5.

Acetamiprid and imidacloprid both belong to the neonicotinoid class of pesticides, but showed different optimum pH values for their maximum degradation using  $\text{Fe}_3\text{O}_4/\text{GO}$ – $\text{Fe}_3\text{O}_4/\text{CoFe}_2\text{O}_4/\text{GO}$ – $\text{CoFe}_2\text{O}_4$  and  $\text{CoFe}_2\text{O}_4$  photocatalyst, respectively. In case of acetamiprid degradation, maximum degradation was achieved at pH 3 [102]. At basic pH values, a decline in photocatalytic activity was observed because of ferrous excess hydroxyl ions reactions. This reaction led to the formation of yellowish-brown ferric hydroxide sludge, which ultimately covered the active sites of the catalyst and hence contributed to the reduction in overall efficiency. The degradation potentials of the catalyst (in all cases) dropped when the pH approached basic values. In the case of the imidacloprid, maximum degradation was achieved at  $\text{pH} > 7.0$ , which may be attributed to the formation of the hydroxide radicals on the surface of  $\text{ZnO}/\text{CoFe}_2\text{O}_4$  magnetic nanocomposite, leading to the degradation of the imidacloprid pesticide [103].

In case of the phenolic compounds, such as phenol, 2-nitrophenol, 2-chlorophenol, p-chlorophenol, 2, 4, and 6-trichlorophenol, maximum degradation occurred in the pH range of 5 to 11, using ammonia modified graphene- $\text{Fe}_3\text{O}_4$ ,  $\text{ZnFe}_2\text{O}_4$  multi-porous microbricks/graphene,  $\text{Fe}_3\text{O}_4@ \beta\text{-CD}$ , and  $\text{Fe}_3\text{O}_4\text{-gC}_3\text{N}_4$  nanocomposites [104–107]. Under alkaline conditions, the interaction between the phenolic compounds and photocatalyst is retarded due to the instability of the oxygen functionalities of the graphene sheets, which

are deprotonated and dissolved in the aqueous medium. Contrary results were obtained for the maximum degradation of the phenol (94.2%), which was achieved at pH 3.5, using manganese ferrite [108]. This may be due to the presence of peroxydisulfate, as its adsorption on the positively charged catalyst surface in the pH range of 3–6 was more intense due to its negatively charged  $\text{SO}_4^-$  radical. In the pH range of 3–7, efficiencies greater than 90% were attained, but at values of pH up to 9, efficiency decreased to 65%.

Thus, the pH of the solution plays a crucial role in the degradation of pollutants. However, the optimum pH for the removal of the organic effluents using ferrites and their nanocomposites as photocatalysts depends upon the type of photocatalyst and the type of organic effluent used.

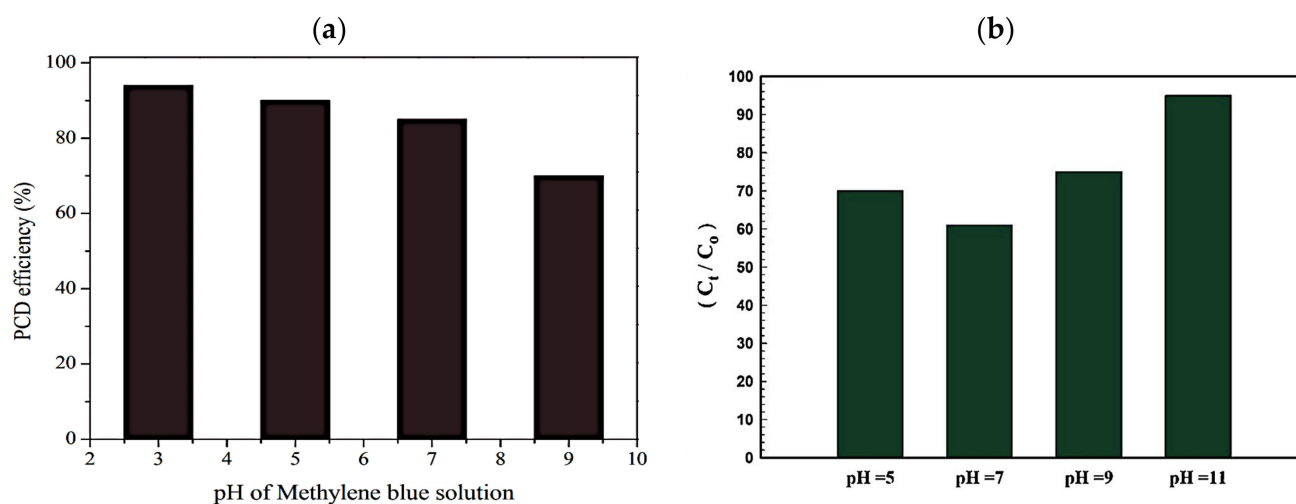


**Figure 3.** (a) Effect of pH on the degradation of methylene blue dye using  $\text{Ni}_x\text{Zn}_{1-x}\text{Fe}_2\text{O}_4$  ( $x = 0.0$  to  $1.0$ ) NPs. Adapted with permission [29]; copyright (2016), Elsevier. (b) Effect of pH on the degradation of Rhodamine B dye using  $\text{Mn}_{0.5}\text{Zn}_{0.125}\text{Mg}_{0.375}\text{Fe}_2\text{O}_4$  NPs. Adapted with permission [100]; copyright (2020), Elsevier.

#### 4.2. Effect of Catalyst Dose

The dose of ferrites used in the photodegradation process is another important parameter. Various studies have reported that the photocatalyst dose is highly related to the degradation of the organic pollutants during photocatalysis [84,109].

The methylene blue dye degradation increased up to a certain level when the magnetic catalyst  $\text{Ni}_{0.6}\text{Zn}_{0.4}\text{Fe}_2\text{O}_4$  loading was increased [29,110]. Furthermore, the negative influence of the catalyst loading on the degradation was observed. The initial rise in the degradation was due to the increase in the number of the active sites present on the surface of the catalyst, increasing the production of  $\cdot\text{OH}$  and  $\text{O}^{2-}\cdot$  radicals. Similar results were reported for the degradation of the methylene blue using  $\text{MFe}_2\text{O}_4$  ( $\text{M} = \text{Co}, \text{Ni}, \text{Cu}, \text{Zn}$ ) and  $\text{ZnFe}_2\text{O}_4$ , respectively [111,112]. The decrease after a certain time was due to either the aggregation of catalyst particles at high concentrations, causing a decrease in the number of surface active sites, or an increase in the opacity and light scattering of the catalyst particles at high concentrations, leading to a decrease. The maximum photodegradation of the methyl orange using  $\text{ZnSm}_{1.5}\text{Fe}_{0.5}\text{O}_4$  photocatalyst was achieved with  $0.1 \text{ g}/100 \text{ mL}$  of catalyst. Unfavourable light scattering and a decrease in the light flow decreased the efficiency of the degradation, even on increasing the amount of catalysts [113]. The ciprofloxacin and remazol deep red dye were degraded using Ru-doped nanoferrites and as a function of the catalyst dosage. The percentage degradation was found to be at a maximum at  $0.50 \text{ gL}^{-1}$  ferrite concentration in both cases. The availability of more catalytic sites was expected to increase the degradation efficiency with increasing catalyst amounts; however, a large amount of ferrite causes turbidity of the solution, which prevents light from reaching the reaction medium and tends to impair the degradation process [101].



Using the  $\text{Mn}_{0.75}\text{Co}_{0.25}\text{Fe}_2\text{O}$  NPs, the effectiveness of the catalyst concentration towards methylene blue degradation after UV light exposure was investigated. The catalyst dose was varied from 10 to 30 mg. It was found that the  $C_t/C_0$  value decreased from 0.14 to 0.05, indicating an improvement in the degradation performance [114]. On increasing the  $\text{Mn}_{0.5}\text{Zn}_{0.125}\text{Mg}_{0.375}\text{Fe}_2\text{O}_4$  photocatalyst dose, it was found that the value of the  $C_t/C_0$  declines from 60 to 50, corresponding to 40% to 50% Rhodamine B removal after 80 min. The higher doses of the catalyst led to an increased absorption of photons by the catalyst, and the degradation efficiency improved (Figure 4a).

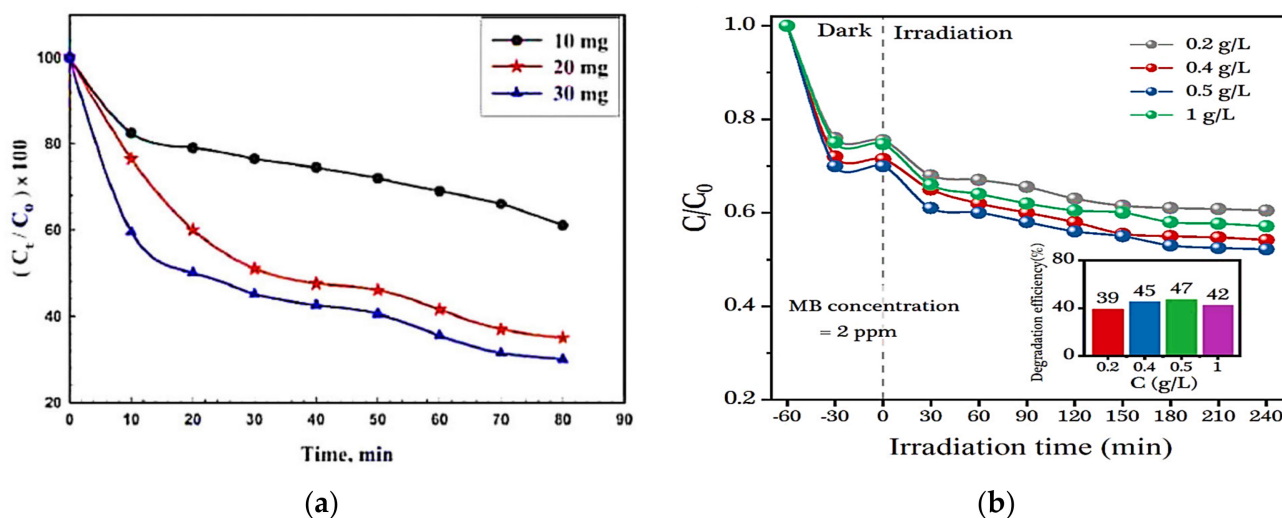


**Figure 4.** (a) Effect of  $\text{Mn}_{0.5}\text{Zn}_{0.125}\text{Mg}_{0.375}\text{Fe}_2\text{O}_4$  dose on the degradation of Rhodamine B dye. Adapted with permission [100]; copyright (2020), Elsevier. (b) Photocatalytic degradation of methylene blue dye as a function of irradiation time at different  $\text{CoFe}_2\text{O}_4/\text{rGO}$  dosages. Inset shows the value of methylene blue dye degradation efficiency as a function of  $\text{CoFe}_2\text{O}_4/\text{rGO}$  dosages. Adapted with permission [115]; copyright (2020), Elsevier.

Similar behavior has been observed while using  $\text{CoFe}_2\text{O}_4/\text{rGO}$  composite as a photocatalyst for the degradation of methylene blue dye [115]. When the catalyst dosage was increased upto  $0.5 \text{ g L}^{-1}$ , the degradation efficiency increased to 47% due to the increased absorption of photons on the surface of the photocatalyst (Figure 4b). However, overdoses of the sample ( $1 \text{ g L}^{-1}$ ) led to falls in the degradation effectiveness. Barium ferrite for the degradation of basic yellow 28, methylene blue, acid orange 7, and basic violet showed similar increases with increases in the catalyst loading from 1 to  $10 \text{ g L}^{-1}$  [76]. The influence of the catalyst dose on the degradation efficiency of acetamiprid was studied by varying the catalyst dose from 0 to  $200 \text{ mg L}^{-1}$ . On increasing the amount of  $\text{GO-Fe}_3\text{O}_4$  and  $\text{GO-CoFe}_2\text{O}_4$  upto certain limit, the degradation increases because of the availability of more catalyst sites for the absorption of light [102]. Effective degradation was achieved for each of the four catalysts, at a catalyst dose of  $100 \text{ mg L}^{-1}$ , and the trend of degrading the acetamiprid was observed increase. However, a further increase in the catalyst concentration led to decreased degradation rates because of the agglomeration of the catalyst.  $\text{CuCe-Ferrite/TiO}_2$  was used for the photodegradation of the reactive red 250 dye, and the efficiency was found to be 100% using  $0.32 \text{ g}/100 \text{ mL}$  of the catalyst. A shift to more wavelength was observed due to the combination of  $\text{CuCe-Ferrite}$  and  $\text{TiO}_2$  and hence the absorption of more visible light [28].

Thus, the photocatalyst dose is an important factor that affects the efficiency of a photocatalyst. In general, it is observed that increasing the photocatalyst dose can lead to a higher efficiency of photo degradation. However, excessively high concentrations can lead to the aggregation of ferrites, which can reduce their efficiency [84].

#### 4.3. Effect of Surface Area of Photocatalyst

The photocatalytic activity of the nanomaterials is enhanced when their surface area is large. The surface area of the nanoparticles is increased with a decrease in particle size, ultimately improving their dispersion in a solution and enhancing their interaction with pollutants. This leads to an improvement in their photocatalytic activity.

The effect of the surface areas of the magnetic NPs system  $\text{Ni}_x\text{Zn}_{1-x}\text{Fe}_2\text{O}_4$ , with different concentrations of  $\text{Ni}^{2+}$  ions ( $0.0 \leq x \leq 1.0$ ), on the photocatalytic degradation of methylene blue was studied [29]. The  $\text{Ni}_{0.6}\text{Zn}_{0.4}\text{Fe}_2\text{O}_4$  was found to have better photocatalytic activity, having a surface area of ( $36.6 \text{ m}^2\text{g}^{-1}$ ) [110]. The particle size and morphology of the  $\text{Cu}_{1-x}\text{Mn}_x\text{Fe}_2\text{O}_4$  effects the photocatalytic degradation of the 4-chlorophenol [116]. For the photodegradation of pendimethalin, core-shell nanocomposites of  $\text{Sr}_{0.4}\text{Ti}_{0.6}\text{Fe}_2\text{O}_{4.6}@\text{SiO}_2$  were used. The increased specific surface area and more active sites observed in the scanning electron and transmission electron micrographs were attributed to the higher photocatalytic efficiency in the core-shell nanocomposites. The highest percentage photodegradation of the pendimethalin was observed in the  $\text{Sr}_{0.4}\text{Ti}_{0.6}\text{Fe}_2\text{O}_{4.6}@\text{SiO}_2$  core-shell nanocomposites, which was found to be 96% [117]. The study on the influence of Zn content on the efficiency of Zn/ $\text{Fe}_2\text{O}_4$  degradation in visible light radiation [118] reported that there was a 40% residual concentration of carbamazepine after an 80-min iron oxide irradiation. On the other hand, the residual carbamazepine concentration decreased as the zinc content increased (Figure 5). Since photocatalytic degradation is a surface-mediated process, the improved degradation efficiency is the result of the increased specific surface area of the zinc-rich nanoparticles [119].

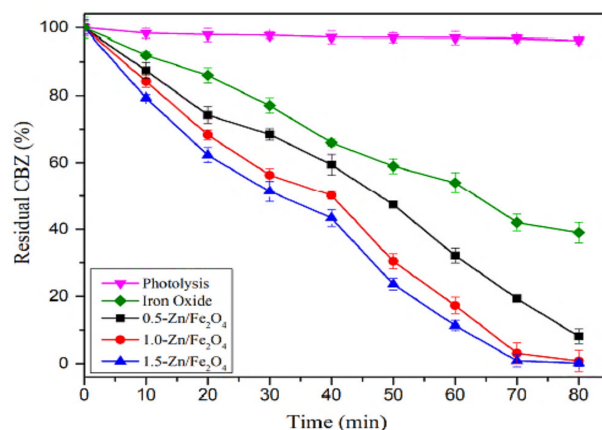


**Figure 5.** Effect of Zn content on the degradation of carbamazepine using  $\text{ZnFe}_2\text{O}_4$  NPs. Adapted with permission [118]; copyright (2021), Elsevier.

The calcination temperature also plays vital role in the increase of the surface area of the photocatalyst. It was observed that on decreasing the calcination temperature of  $\text{MgFe}_2\text{O}_4$  from  $600^\circ\text{C}$  to  $500^\circ\text{C}$ , the particle size of the NPs increased which in turn increased the surface area and ultimately enhanced the photocatalytic activity [120]. The removal of the basic yellow 28, methylene blue, acid orange 7, and basic violet has been studied using barium ferrite composite [76]. The complete decomposition of the dye was observed using  $1000^\circ\text{C}$  sintered catalyst, while catalysts that were sintered at  $700^\circ\text{C}$  or  $800^\circ\text{C}$  degraded only 30% of the dye. The superior removal efficiency of the catalyst sintered at  $1000^\circ\text{C}$  was due to presence of more barium ferrite phase. On the contrary, the degradation of the congo red, methyl orange, methylene blue, Rhodamine B, 4-nitrophenol, and 4-chlorophenol using the  $\text{CoFe}_2\text{O}_4$  xerogel was found to decrease from 96% to 75% when it was calcined at a temperature range of  $500\text{--}900^\circ\text{C}$ . As the calcining temperature rose, the rate of degradation of the nano- $\text{CoFe}_2\text{O}_4$  photocatalyst decreased, which was related to the BET-specific surface area of the  $\text{CoFe}_2\text{O}_4$  NPs [121].

Hence, the particle size, surface area, and availability of the active sites are very important characteristics for enhancing photocatalytic properties. Small particle sizes with high crystallinity are crucial in this regard because their higher specific surface area encourages greater photocatalytic activity. Sometimes, synthesizing at a high temperature is necessary to create particles with a high crystallinity, but it also increases the particle size. As a result, one must consider how to maximize crystallinity without sacrificing particle size [122].

#### 4.4. Effect of Substrate Concentration

The dependence of the substrate concentration on the photocatalytic reaction rate is an important factor. The photocatalytic degradation was the highest for 10 mg·L<sup>-1</sup> of dye concentration, which decreased on further increasing the methyl orange concentration from 10 to 30 mg L<sup>-1</sup> due to absorption of solar light by the dye [113]. A contradictory behavior was observed while using the CoFe<sub>2</sub>O<sub>4</sub>/rGO photocatalyst for the methylene blue [115]. The photocatalytic efficiency of the CoFe<sub>2</sub>O<sub>4</sub>/rGO photocatalyst increased from 47 to 55% on raising the initial dye concentration from 2 to 5 mg·L<sup>-1</sup> and decreased to 45% for 15 mg·L<sup>-1</sup>. The strong interactions between the nanocomposite and dye molecules were responsible for the initial rise in the degradation efficiency (Figure 6). However, lesser photons adsorption by the photocatalyst due to the increase in the methylene blue dye decreased the activity of the catalyst. Similar behavior was observed in MFe<sub>2</sub>O<sub>4</sub> (M = Co, Ni, Cu, Zn) for the degradation of the methylene blue upto 94% using 20 mg·L<sup>-1</sup> of photocatalyst. The efficiency decreased to 65% for a 50 mg·L<sup>-1</sup> methylene blue solution. However, the limited production of the active radicals, which were insufficient to degrade the higher concentration of the methylene blue dye, was the main factor in the outcome. The photogeneration of the electron-hole pairs was also hampered by the highly concentrated methylene blue dye solution, as it reduced photon penetration in the solution phase [111]. Similar results were observed during the degradation of the methylene blue dye using CuFe<sub>2</sub>O<sub>4</sub>/TiO<sub>2</sub> and ZnFe<sub>2</sub>O<sub>4</sub> [109,112].

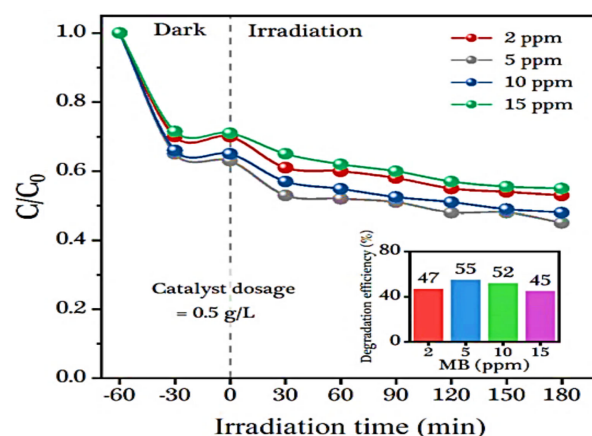


**Figure 6.** Photocatalytic degradation of methylene blue dye as a function of irradiation time at different substrate concentration. Inset shows the value of methylene blue degradation efficiency as a function of substrate concentration. Adapted with permission [115]; copyright (2020), Elsevier.

The effect of the substrate concentration on the photodegradation of reactive red 250 dye using TiO<sub>2</sub> and CuCe-Ferrite/TiO<sub>2</sub> NPs has been examined [28]. When the concentration of the reactive red 250 was increased to 100 ppm, a decrease in the chemical oxygen demand was observed over TiO<sub>2</sub> and CuCe-Ferrite/TiO<sub>2</sub> NPs. These observations were correlated to a decrease in the light penetration because an increase in the reactive red 250 dye concentration resulted in the incorporation of additional reactive red 250 dye molecules onto the TiO<sub>2</sub> and CuCe-Ferrite/TiO<sub>2</sub> NPs. The Fe<sub>3</sub>O<sub>4</sub>, GOFe<sub>3</sub>O<sub>4</sub>, CoFe<sub>2</sub>O<sub>4</sub>, and GO-CoFe<sub>2</sub>O<sub>4</sub> effectively (80%) degraded 10 mg·L<sup>-1</sup> solution of acetamiprid. The degradation efficiency was observed to be 100% on increasing the acetamiprid from 2 to

$8 \text{ mg}\cdot\text{L}^{-1}$ . However, as the pesticide dose was increased from  $10 \text{ mg}\cdot\text{L}^{-1}$  to  $16 \text{ mg}\cdot\text{L}^{-1}$ , more active sites were occupied due to the increased addition of pollutant molecules [102].

#### 4.5. Effect of Irradiation Intensity and Time

The intensity of the irradiation is another important factor responsible for the photodegradation process. The effect of the irradiation intensity has been studied for the photocatalytic degradation of basic yellow 28, methylene blue, acid orange 7, basic violet using barium ferrite, and rGO composite [76]. With an increase in the irradiation intensity from 3500 to 15,000 lx, the degradation efficiency went from 3 to 25%. The degradation rose to 47.4% with an additional increase in the irradiation intensity to 26,000 lx. The clear indication that the catalyst activity was based on photocatalysis rather than any other assumed mechanisms was due to the sizeable increase in degradation with irradiation intensity. At higher irradiation intensities, the catalyst surface was exposed to more photons, which can be used to fuel the degradation process.

The effect of irradiation time has been studied for the photodegradation of methylene blue using  $\text{CoFe}_2\text{O}_4/\text{rGO}$ . The degradation efficiency increased on increasing the irradiation time to 180 min with catalyst dosage of  $0.5 \text{ g}\cdot\text{L}^{-1}$ , and a methylene blue dye concentration of  $5 \text{ mg}\cdot\text{L}^{-1}$  reached a relatively stable value [115] (Figures 4b and 6).  $\text{ZnFe}_2\text{O}_4$  NPs were used to measure the rate of the methylene blue dye decomposition over time. When the dye was exposed to UV light, the degradation increased (99.8%) with longer exposure times, up to 45 min. A plateau was reached after 45 min because the degradation did not increase [112].

A rapid increase in the degradation of acetamiprid was observed when the irradiation time was varied from 15 to 120 min and studied at an ideal pH, oxidant dose, dose of pesticide, and catalyst. The rate slowed down with time, and the active sites required 60 min to completely degrade the pollutant [102]. When the magnesium ions were doped in the cobalt ferrite NPs at various fractions, the rate of photo degradation increased and the degradation time fell to 225 min, which was 330 min for the pure cobalt ferrite. An increase in the  $\text{Mg}^{2+}$  concentration decreases the rate of degradation due to the consequent increase in the number of active sites on the surface of the photocatalyst [123].

#### 4.6. Effect of Doping

The doping of ferrites is also emerging as a new method for enhancing photocatalytic potential, as doped ferrites display enhanced visible light absorption and improved photodegradation efficiency towards various types of organic pollutants [122].

The effectiveness of  $\text{MRu}_x\text{Fe}_{2-x}\text{O}_4$  ( $\text{M} = \text{Ni}, \text{Cu}$ ) NPs was assessed for remazol deep red and ciprofloxacin photocatalytic degradation [101]. With an increasing Ru content, the catalytic activity of the  $\text{MRu}_x\text{Fe}_{2-x}\text{O}_4$  ( $x = 0, 0.02, 0.06, 0.1, \text{ and } 0.4$ ) increased. The  $\text{NiRu}_{0.4}\text{Fe}_{1.6}\text{O}_4$  demonstrated the best catalytic performance, with complete degradation in 5 min. When the Ru was substituted, the increased catalytic activity supported the preference for the octahedral site. The  $\text{CuRu}_x\text{Fe}_{2-x}\text{O}_4$  showed an increase in the photocatalytic efficiency, which was found to be 92% for  $x = 0.02$ , whereas with further substitution up to  $x = 0.06$  and  $x = 0.1$ , the degradation time reached 120 min and 90 min, respectively. Similarly, when the Ti content in the ternary-doped  $\text{Sr}_{1-x}\text{Ti}_x\text{Fe}_2\text{O}_{4+\delta}$  ferrite was increased from 0.3 to 0.6, the band gap was decreased from 2.45 to 2.18 eV, which increased the charge carrier concentration and decreased the barrier height from 1.20 to 1.02 eV, compared to the pure  $\text{SrFe}_2\text{O}_4$  and  $\text{TiFe}_2\text{O}_5$  [83]. These features were very helpful for the degradation of the p-nitrophenol, pendimethalin and martius yellow with apparent rate constant values  $1.9 \times 10^{-2} \text{ min}^{-1}$ ,  $2.3 \times 10^{-2} \text{ min}^{-1}$ , and  $1.3 \times 10^{-2} \text{ min}^{-1}$ , respectively. Similar results have been reported for the degradation of rhodamine B dye [124].

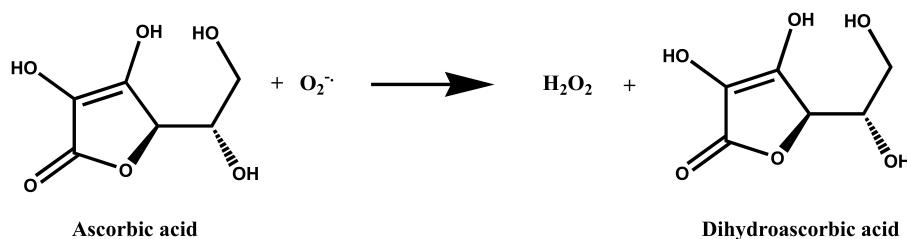
Furthermore, doping  $\text{Y}^{3+}$  into pure  $\text{CoFe}_2\text{O}_4$  has improved the stability of the composite and increased photocatalytic activity compared to that of pure  $\text{CoFe}_2\text{O}_4$  NPs [125]. The doping increased the stability and effectiveness of the  $\text{CoFe}_2\text{O}_4$  NPs when exposed to visible light. However, higher concentrations of metal ions may cause the photocat-

alyst to lose its crystallite and have more internal defects. As a result, it decreased the efficiency of the photocatalytic system. Moreover, the photocatalytic activity was increased by using rare earth metals such as  $\text{Dy}^{3+}$ ,  $\text{Nd}^{3+}$ ,  $\text{Eu}^{3+}$ ,  $\text{Gd}^{3+}$ , and others as dopants [126]. The photocatalytic efficiency increased, while the energy band gap decreased (1.95 to 1.42) when the  $\text{Sm}^{3+}$  was doped into the pure  $\text{ZnFe}_2\text{O}_4$  ( $\text{ZnSm}_x\text{Fe}_{2-x}\text{O}_4$ ). High photocatalytic degradation of methyl orange was observed when the  $\text{ZnSm}_{1.5}\text{Fe}_{0.5}\text{O}_4$  NPs were used as a photocatalyst. After 80 min, 92.3% of the degradation was observed [113].

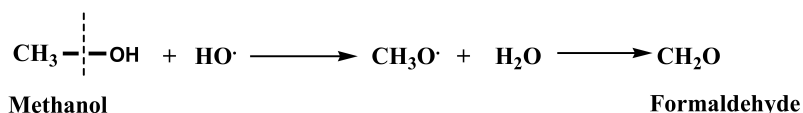
Generally, the doping of ferrites causes a narrowing of the band gap, which aids in in the absorption of lower energy photons and trapping of electrons [127–129]. This renders them a superior visible light active photocatalyst compared to the other nanomaterials. However, it is difficult to predict the best kind of dopant, as their efficiency can change with changes in other operational parameters.

#### 4.7. Effect of Quenchers

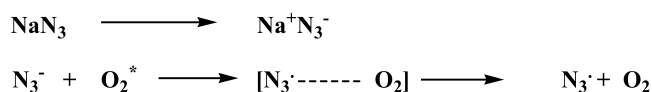
In order to conclude the probable photocatalytic degradation mechanism of different organic pollutants over the photocatalyst surface, various quenchers have been added to study the quenching effect. It has been observed that the use of various scavengers decreases the photocatalytic degradation efficiencies [28]. Different quenchers, such as ethylene diamine tetraacetate (EDTA,  $\text{h}^+$  scavenger), methanol/butanol ( $\text{CH}_3\text{OH}/\text{C}_4\text{H}_9\text{OH}$ ,  $\bullet\text{OH}$  scavenger), ascorbic acid ( $\text{C}_6\text{H}_8\text{O}_6$ ,  $\bullet\text{O}_2^-$  scavenger), and sodium azide ( $\text{NaN}_3$ ,  $\text{O}_2^*$  species) work according to the following reactions:



Ascorbic acid acts as an electron donor and converts superoxide radical ( $\bullet\text{O}_2^-$ ) into hydrogen peroxide ( $\text{H}_2\text{O}_2$ ).



Hydroxyl radical ( $\text{HO}\bullet$ ) abstracts hydrogen from methanol and converted into formaldehyde. In this way, methanol quenches hydroxyl radicals.



Singlet oxygen forms charge transfer complex with  $\text{N}_3^-$  which ultimately decomposes into  $\text{N}_3$  radical.

Various studies based on photocatalysis have demonstrated that out of ethylene diamine tetraacetate, methanol/butanol, ascorbic acid, and sodium azide, ascorbic acid possesses the highest inhibiting effect, which means that the  $\bullet\text{O}_2^-$  radicals were primary species responsible for the degradation of the organic pollutants [84,117,130]. The addition of ascorbic acid greatly quenched (61.8%) the photodegradation of the martius yellow, followed by the butanol (73.7%), ethylene diamine tetraacetate (92.3%) and methanol (90.9%), using magnesium ferrite-bentonite as a photocatalyst [88]. This might be due to the increase in the number of the hydroxyl radicals in the presence of hydrogen peroxide, a potent oxidising agent [114]. A similar quenching effect was studied for methyl orange and tetracycline degradation [131].

However, a limited number of papers have been published addressing the effect of quenchers on the degradation of organic pollutants. Thus, clear insight about the influence of quenchers has not been explored yet.

#### 4.8. Photodegradation Mechanism

Photocatalysis using ferrite-based nanomaterials as photocatalysts involves the interaction of photons of light to breakdown various organic pollutants [132–136]. They consist of semiconductors with large bandgaps where electrons are readily promoted from valence into the conduction band after the absorption of photons. This results in the generation of photoexcited electrons ( $e^-$ ) and positive-valence band holes ( $h^+$ ). The photocatalytic mechanism of degradation works through pollutants being reduced or oxidized by photoexcited electrons ( $e^-$ ) and holes ( $h^+$ ). In water, hydroxide ( $^-OH$ ) ions (generated when positive-valence band holes ( $h^+$ ) are trapped by water) are non-selective strong oxidizing agents that oxidize organic pollutants to water and gaseous products. Similarly, photoexcited electrons can react with  $O_2$  to form other reactive oxygen species that can be used to further degrade pollutants [132,137]. The photocatalytic degradation of organic pollutants, such as rhodamine B, imidacloprid, and acetamiprid, has been reported for Ag/AgBr/NiFe<sub>2</sub>O<sub>4</sub> and ZnO/CoFe<sub>2</sub>O<sub>4</sub> [138–141].

In the case of doped ferrite NPs, the doped element enhances the photocatalytic potential of the pristine ferrite materials; for example, cerium doping in cobalt ferrite NPs plays the important role of electron scavenger [141]. The interfacial electron transfer, photo-excited charge generation, and inhibition of ( $e^-$ - $h^+$ ) recombination were completely dependent on the Ce 4f level (Equation (1)). The electron-scavenging efficiency of Ce<sup>4+</sup> helps to capture the conduction-band electrons, and due to its Lewis acidic nature, it was found to be more effective at trapping electrons compared to the molecular oxygen (Equation (2)). Through an oxidation process (Equation (3)), the electron was transferred to the adsorbed  $O_2$ , and superoxide radical anions ( $-O_2^-$ ) were formed [115]. These reactive oxygen species helped in the degradation of the RhB dye.



Meanwhile, the  $H_2O$  molecules can easily scavenge  $h^+$  to produce  $-OH$  radicals (Equation (4)). The rhodamine B dye can be decomposed into  $CO_2$ ,  $H_2O$ , and mineral acids.

The incorporation of ferrites into ultraviolet and visible light active metal oxides, polymers, carbon materials, etc. is another way to photodegrade organic pollutants. Figure 7 depicts the transfer of the photogenerated electrons of the metal oxide and ferrites nanocomposites from the conduction band of the one photocatalyst to the other, while holes are jumped from the valence band of the photocatalyst-II to the photocatalyst-I. Reactive species are created as a result of the efficient separation of the electron-hole pair [142–147].

The recovery of carbon-based materials is quite difficult due to their poor visible light absorption properties, which decrease their efficiency as photocatalysts for the removal of organic pollutants from wastewater. However, they are viewed as potential resources for improving the efficiency of MFe<sub>2</sub>O<sub>4</sub> as a photocatalyst. Reduced graphene oxide sheets act as an electron trap center, which, as shown in Figure 8a, significantly enhances the photocatalytic activity of the MFe<sub>2</sub>O<sub>4</sub> nanoparticles [148–151].

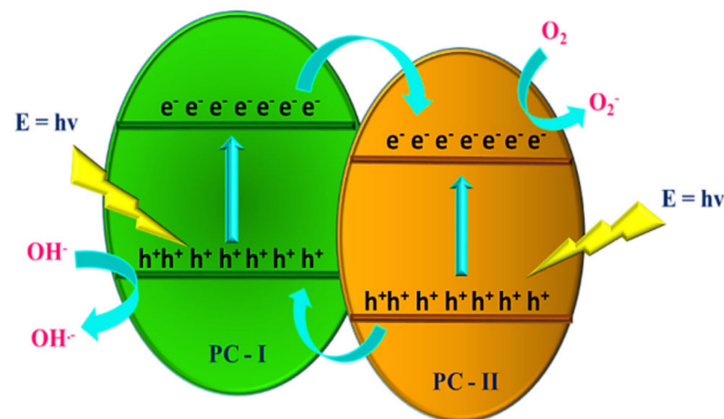


**Figure 7.** Pathway for photogenerated charges transfer between metal oxide and ferrite under visible light with wide band gap. PC–I: photocatalyst 1 and PC–II: photocatalyst 2.

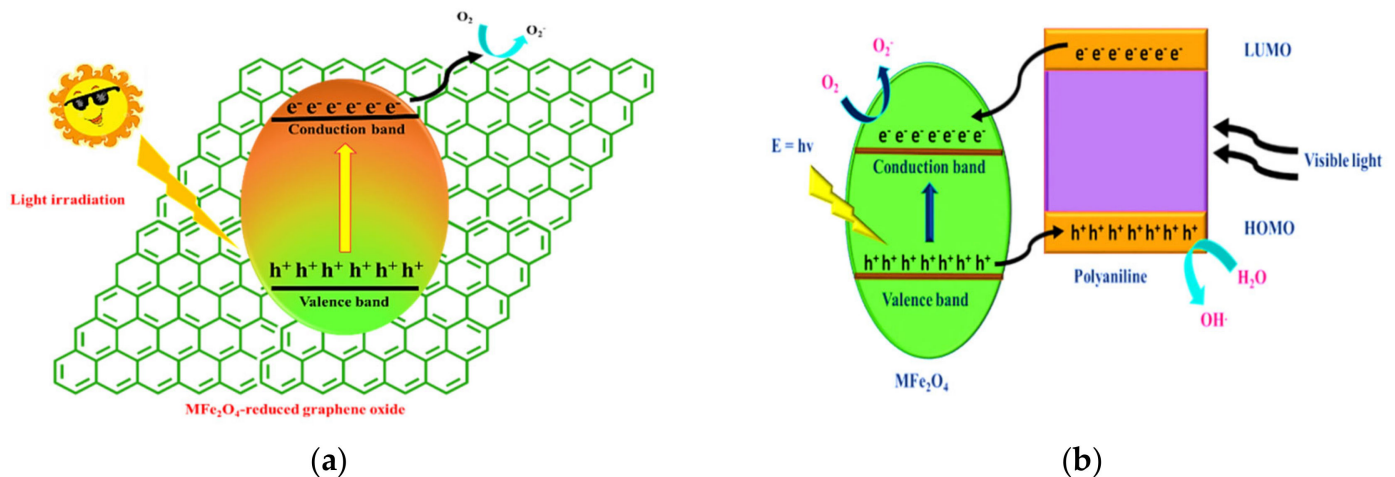


**Figure 8.** (a): Production for free radicals mechanism under visible light by ferrite/reduced graphene oxide nanocomposite. (b): Free radicals generation mechanism under visible light by spinel ferrite/polymer nanocomposite. HOMO—highest occupied molecular orbital and LUMO—lowest unoccupied molecular orbital.

Polymers, such as polyaniline, are another type of supporting material. The positions of the highest and lowest occupied molecular orbitals (HOMO and LUMO) are  $-1.9$  and  $0.8$  eV, respectively, as depicted in Figure 8b. When exposed to visible light, polyaniline on absorption undergoes  $\pi$ - $\pi^*$  transition. When the excited electron in the lowest occupied molecular orbital is transferred to the conduction band, it produces the reactive species, which are responsible for degrading the organic pollutants [152,153].

Ferrite NPs are also combined with a variety of materials, such as metal sulphide [154], metal phosphate [155], metal oxyhalide [156], metal vanadate [3], metal titanate [157], etc., which makes their degradation mechanism different.  $\text{MgFe}_2\text{O}_4/\text{Bi}_2\text{MoO}_6$  composites have been used to degrade malachite green dye [158]. Free radicals were produced through the Z-scheme mechanism, as shown in Figure 9. Due to the difference in the band gaps of the  $\text{MgFe}_2\text{O}_4$  and  $\text{Bi}_2\text{MoO}_6$ , photogenerated electrons from the conduction band of the latter material diffuse to the valence band and become effectively trapped. Radicals produced by photogenerated holes and electrons, such as hydroxyl and superoxide, are also involved in the photodegradation process. Using the  $\text{SnFe}_2\text{O}_4/\text{ZnFe}_2\text{O}_4$  heterostructure, the degradation of tetracycline observed followed the S-scheme mechanism (Figure 9), where holes in the valence band of the  $\text{SnFe}_2\text{O}_4$  were neutralised by the photogenerated electrons in the  $\text{ZnFe}_2\text{O}_4$  [159]. As a result, the availability of holes in the  $\text{ZnFe}_2\text{O}_4$  and electrons in the  $\text{SnFe}_2\text{O}_4$  makes the production of hydroxyl and superoxide radicals possible.

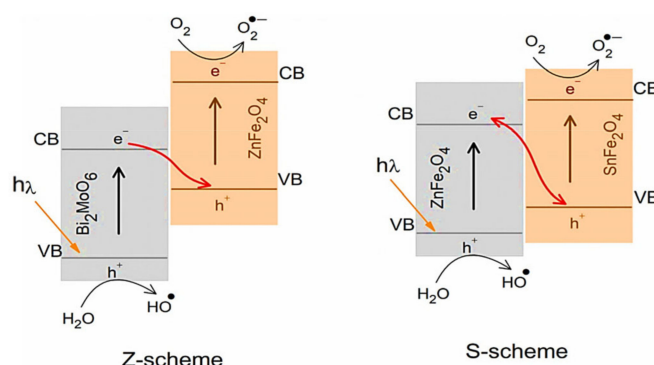


**Figure 9.** Free radicals production using S-scheme and Z-scheme mechanisms. Adapted with permission [159]; copyright (2021), Elsevier.

#### 4.9. Reusability and Stability

The ideal photocatalyst is one that is reusable and has high photocatalytic efficiency under visible light [160]. Therefore, one of the crucial steps is to recycle photocatalysts for the development of heterogeneous photocatalysis. Recent research has shown that magnetic nanoparticles can be successfully recycled using magnetic separation techniques [161–165].

Five consecutive cycles of photodegradation were conducted to examine the stability of  $\text{Sr}_{0.4}\text{Ti}_{0.6}\text{Fe}_2\text{O}_{4.6}@\text{SiO}_2$ . A slight decrease (<7.0%) in the photocatalytic efficiency of pendimethalin was found after five runs, which was due to adsorption of the intermediate product on the surface of the photocatalyst where active sites are blocked [117]. Similar results were found when the hierarchical nanoflowers of the  $\text{MgFe}_2\text{O}_4$ , Bentonite and B-, P-co-doped Graphene Oxide were tested for their reusability and stability. The degradation efficiency was found to be decreased by only 5% after 5 consecutive cycles [83].

Generally, most of the magnetic nanocomposites can be reused upto three to four cycles, demonstrating their reusability when used for the photodegradation of pollutants from wastewater [75,101,112,166].

## 5. Conclusions and Future Perspective

In this review, the impact of different parameters on the photocatalytic degradation of organic effluents using ferrites and their nanocomposites has been elaborated. Different types of photodegradation mechanisms of ferrites and their nanocomposites are discussed. The use of visible light sensitive ferrite-based nanomaterials as photocatalysts for the remediation of wastewater and degradation of organic contaminants like pharmaceuticals, phenols, dyes, and other persistent organic pollutants is one of the most active research areas at the moment. The bulk synthesis of ferrite nanoparticles is needed for practical applications. Using chemical methods, the yield of ferrites is low, whereas physical methods yield ferrites in bulk but in micrometer regime. Future research can be focused on the bulk synthesis of ferrites using green and atomically efficient chemical methods and facile physical methods that can yield ferrites in nanometer range. Moreover, while evaluating the degradation efficacy of a photocatalyst, the pollutant concentration must always be taken into account, regardless of the pollutant that is intended to be removed. So, predicting the pollutant concentration and optimization of the catalyst dose must therefore be taken into account. Generally, ferrites and their nanocomposites, due to their appealing properties, such as their ease of surface modification and stability, are promising nanomaterials for addressing a variety of issues. Even though there have been many studies on ferrites, more research is needed on different parameters that affect the degradation of various organic pollutants under visible light, and technology having the potential to optimize the influential parameters is needed for the photocatalysis process to be more economical.

**Author Contributions:** Writing—original draft preparation, G.S., M.K., K.J., M.K.U. and C.S.; Writing—review and editing, G.S., M.K., K.J., M.K.U. and C.S.; Supervision, M.K., K.J. and C.S. All authors have read and agreed to the published version of the manuscript.



**Funding:** This research received no external funding.

**Institutional Review Board Statement:** Not applicable.

**Informed Consent Statement:** Not applicable.

**Data Availability Statement:** Not applicable.

**Conflicts of Interest:** The authors declare no conflict of interest.

## References

1. Anh, H.Q.; Le, T.P.Q.; Da Le, N.; Lu, X.X.; Duong, T.T.; Garnier, J.; Rochelle-Newall, E.; Zhang, S.; Oh, N.-H.; Oeurng, C.; et al. Antibiotics in surface water of East and Southeast Asian countries: A focused review on contamination status, pollution sources, potential risks, and future perspectives. *Sci. Total Environ.* **2020**, *764*, 142865. [[CrossRef](#)] [[PubMed](#)]
2. Show, P.L.; Ooi, C.W.; Anuar, M.S.; Ariff, A.; Yusof, Y.A.; Chen, S.K.; Annuar, M.S.M.; Ling, T.C. Recovery of lipase derived from *Burkholderiacenocepacia* ST8 using sustainable aqueous two-phase flotation composed of recycling hydrophilic organic solvent and inorganic salt. *Sep. Purif. Technol.* **2013**, *110*, 112–118. [[CrossRef](#)]
3. Sakhare, P.A.; Pawar, S.S.; Bhat, T.S.; Yadav, S.D.; Patil, G.R.; Patil, P.S.; Sheikh, A.D. Magnetically Recoverable BiVO<sub>4</sub>/NiFe<sub>2</sub>O<sub>4</sub> Nanocomposite Photocatalyst for Efficient Detoxification of Polluted Water Under Collected Sunlight. *Mater. Res. Bull.* **2020**, *129*, 110908. [[CrossRef](#)]
4. Saxena, G.; Bharagava, R. Organic and Inorganic Pollutants in Industrial Wastes: Ecotoxicological Effects, Health Hazards, and Bioremediation Approaches. In *Environmental Pollutants and Their Bioremediation Approaches*; Bharagava, R., Ed.; CRC Press: Boca Raton, FL, USA, 2017; pp. 23–56. ISBN 9781138628892.
5. Uday, U.; Mahata, N.; Sasmal, S.; Bandyopadhyay, T.; Mondal, A.; Bhunia, B. Dyes Contamination in the Environment: Ecotoxicological Effects, Health Hazards, and Biodegradation and Bioremediation Mechanisms for Environmental Cleanup. In *Environmental Pollutants and Their Bioremediation Approaches*; Bharagava, R., Ed.; CRC Press: Boca Raton, FL, USA, 2017; pp. 127–176. ISBN 9781138628892.
6. Koduru, J.; Shankar, S.; More, N.; Shikha; Lingamdinne, L.; Singh, J. Toxic Metals Contamination in the Environment: Toxicological Effects and Bioremediation Approaches for Environmental Cleanup. In *Environmental Pollutants and Their Bioremediation Approaches*; Bharagava, R., Ed.; CRC Press: Boca Raton, FL, USA, 2017; pp. 209–240. ISBN 9781138628892.
7. Karimi-Maleh, H.; Alizadeh, M.; Orooji, Y.; Karimi, F.; Baghayeri, M.; Rouhi, J.; Tajik, S.; Beitollahi, H.; Agarwal, S.; Gupta, V.K.; et al. Guanine-Based DNA Biosensor Amplified with Pt/SWCNTs Nanocomposite as Analytical Tool for Nanomolar Determination of Daunorubicin as an Anticancer Drug: A Docking/Experimental Investigation. *Ind. Eng. Chem. Res.* **2021**, *60*, 816–823. [[CrossRef](#)]
8. Deliyanni, E.A.; Kyzas, G.Z.; Matis, K.A. Various flotation techniques for metal ions removal. *J. Mol. Liq.* **2016**, *225*, 260–264. [[CrossRef](#)]
9. Yu, K.L.; Show, P.L.; Ong, H.C.; Ling, T.C.; Lan, J.C.-W.; Chen, W.-H.; Chang, J.-S. Microalgae from wastewater treatment to biochar—Feedstock preparation and conversion technologies. *Energy Convers. Manag.* **2017**, *150*, 1–13. [[CrossRef](#)]
10. Chua, S.F.; Nouri, A.; Ang, W.L.; Mahmoudi, E.; Mohammad, A.W.; Benamor, A.; Ba-Abbad, M. The emergence of multifunctional adsorbents and their role in environmental remediation. *J. Environ. Chem. Eng.* **2021**, *9*, 104793. [[CrossRef](#)]
11. Liu, Y.; Deng, Y.-Y.; Zhang, Q.; Liu, H. Overview of recent developments of resource recovery from wastewater via electrochemistry-based technologies. *Sci. Total Environ.* **2021**, *757*, 143901. [[CrossRef](#)]
12. Hansima, M.A.C.K.; Makehelwala, M.; Jinadasa, K.B.S.N.; Wei, Y.; Nanayakkara, K.G.N.; Herath, A.C.; Weerasooriya, R. Fouling of ion exchange membranes used in the electrodialysis reversal advanced water treatment: A review. *Chemosphere* **2021**, *263*, 127951. [[CrossRef](#)]
13. Ajiboye, T.O.; Oyewo, O.A.; Onwudiwe, D.C. Simultaneous removal of organics and heavy metals from industrial wastewater: A review. *Chemosphere* **2021**, *262*, 128379. [[CrossRef](#)]
14. Arshad, Z.I.M.; Amid, A.; Yusof, F.; Jaswir, I.; Ahmad, K.; Loke, S.P. Bromelain: An overview of industrial application and purification strategies. *Appl. Microbiol. Biotechnol.* **2014**, *98*, 7283–7297. [[CrossRef](#)]
15. Naushad, M.; Sharma, G.; Alothman, Z.A. Photodegradation of toxic dye using Gum Arabic-crosslinked-poly(acrylamide)/Ni(OH)<sub>2</sub>/FeOOH nanocomposites hydrogel. *J. Clean. Prod.* **2019**, *241*, 118263. [[CrossRef](#)]
16. Faisal, A.A.H.; Al-Wakel, S.F.A.; Assi, H.A.; Naji, L.A.; Naushad, M. Waterworks sludge-filter sand permeable reactive barrier for removal of toxic lead ions from contaminated groundwater. *J. Water Process Eng.* **2020**, *33*, 101112. [[CrossRef](#)]
17. Mironyuk, I.; Tatarchuk, T.; Naushad, M.; Vasylyeva, H.; Mykytyn, I. Highly efficient adsorption of strontium ions by carbonated mesoporous TiO<sub>2</sub>. *J. Mol. Liq.* **2019**, *285*, 742–753. [[CrossRef](#)]
18. Chen, C.; Duan, F.; Zhao, S.; Wang, W.; Yang, F.; Nuansing, W.; Zhang, B.; Qin, Y.; Knez, M. Porous Fe<sub>2</sub>O<sub>3</sub> nanotubes with  $\alpha$ - $\gamma$  phase junction for enhanced charge separation and photocatalytic property produced by molecular layer deposition. *Appl. Catal. B Environ.* **2019**, *248*, 218–225. [[CrossRef](#)]
19. Crini, G.; Lichtfouse, E. Advantages and disadvantages of techniques used for wastewater treatment. *Environ. Chem. Lett.* **2019**, *17*, 145–155. [[CrossRef](#)]

20. Ong, C.B.; Ng, L.Y.; Mohammad, A.W. A review of ZnO nanoparticles as solar photocatalysts: Synthesis, mechanisms and applications. *Renew. Sustain. Energy Rev.* **2018**, *81*, 536–551. [[CrossRef](#)]
21. Khalid, N.R.; Majid, A.; Tahir, M.B.; Niaz, N.A.; Khalid, S. Carbonaceous-TiO<sub>2</sub> nanomaterials for photocatalytic degradation of pollutants: A review. *Ceram. Int.* **2017**, *43*, 14552–14571. [[CrossRef](#)]
22. Jiang, M.; Zhang, M.; Wang, L.; Fei, Y.; Wang, S.; Núñez-Delgado, A.; Bokhari, A.; Race, M.; Khataee, A.; Klemeš, J.J.; et al. Photocatalytic degradation of xanthate in flotation plant tailings by TiO<sub>2</sub>/graphene nanocomposites. *Chem. Eng. J.* **2022**, *431*, 134104. [[CrossRef](#)]
23. Hitam, C.N.C.; Jalil, A.A.; Abdurashheed, A.A. A review on recent progression of photocatalytic desulphurization study over decorated photocatalysts. *J. Ind. Eng. Chem.* **2019**, *74*, 172–186. [[CrossRef](#)]
24. Byrne, C.; Subramanian, G.; Pillai, S.C. Recent advances in photocatalysis for environmental applications. *J. Environ. Chem. Eng.* **2018**, *6*, 3531–3555. [[CrossRef](#)]
25. Khaki, M.R.D.; Shafeeyan, M.S.; Raman, A.A.A.; Daud, W.M.A.W. Application of doped photocatalysts for organic pollutant degradation—A review. *J. Environ. Manag.* **2017**, *198*, 78–94. [[CrossRef](#)]
26. Danish, M.S.S.; Estrella, L.L.; Alemaida, I.M.A.; Lisin, A.; Moiseev, N.; Ahmadi, M.; Nazari, M.; Wali, M.; Zaheb, H.; Senjyu, T. Photocatalytic Applications of Metal Oxides for Sustainable Environmental Remediation. *Metals* **2021**, *11*, 80. [[CrossRef](#)]
27. Chakkunni, A.H.; Thomas, B.; Alexander, L.K. Influence of pH and salinity on the photocatalytic dye degradation and heavy metal ion reduction with cobalt ferrite photocatalysts. *IOP Conf. Ser. Mater. Sci. Eng.* **2021**, *1187*, 012018. [[CrossRef](#)]
28. Helmy, E.T.; Soliman, U.A.; Elbasiony, A.M.; Nguyen, B.-S. CuCe-Ferrite/TiO<sub>2</sub> Nanocomposite as an Efficient Magnetically Separable Photocatalyst for Dye Pollutants Decolorization. *Top. Catal.* **2023**, *66*, 53–63. [[CrossRef](#)]
29. Padmapriya, G.; Manikandan, A.; Krishnasamy, V.; Jaganathan, S.K.; Antony, S.A. Spinel Ni Zn<sub>1</sub>Fe<sub>2</sub>O<sub>4</sub> (0.0 ≤ x ≤ 1.0) nanoprecipitates: Synthesis, characterization and photocatalytic degradation of methylene blue dye. *J. Mol. Struct.* **2016**, *1119*, 39–47. [[CrossRef](#)]
30. Haruna, A.; Abdulkadir, I.; Idris, S.O. Photocatalytic activity and doping effects of BiFeO<sub>3</sub> nanoparticles in model organic dyes. *Heliyon* **2020**, *6*, e03237. [[CrossRef](#)]
31. Oliveira, T.P.; Marques, G.N.; Castro, M.A.M.; Costa, R.C.V.; Rangel, J.H.G.; Rodrigues, S.F.; dos Santos, C.C.; Oliveira, M.M. Synthesis and photocatalytic investigation of ZnFe<sub>2</sub>O<sub>4</sub> in the degradation of organic dyes under visible light. *J. Mater. Res. Technol.* **2020**, *9*, 15001–15015. [[CrossRef](#)]
32. Hitam, C.; Jalil, A. A review on exploration of Fe<sub>2</sub>O<sub>3</sub> photocatalyst towards degradation of dyes and organic contaminants. *J. Environ. Manag.* **2020**, *258*, 110050. [[CrossRef](#)]
33. Ji, J.; Huang, Y.; Yin, J.; Zhao, X.; Cheng, X.; He, S.; Li, X.; He, J.; Liu, J. Synthesis and Electromagnetic and Microwave Absorption Properties of Monodisperse Fe<sub>3</sub>O<sub>4</sub>/α-Fe<sub>2</sub>O<sub>3</sub> Composites. *ACS Appl. Nano Mater.* **2018**, *1*, 3935–3944. [[CrossRef](#)]
34. Saif, S.; Tahir, A.; Asim, T.; Chen, Y.; Adil, S.F. Polymeric Nanocomposites of Iron–Oxide Nanoparticles (IONPs) Synthesized Using *Terminalia chebula* Leaf Extract for Enhanced Adsorption of Arsenic(V) from Water. *Colloids Interfaces* **2019**, *3*, 17. [[CrossRef](#)]
35. Arias, L.S.; Pessan, J.P.; Vieira, A.P.M.; de Lima, T.M.T.; Delbem, A.C.B.; Monteiro, D.R. Iron Oxide Nanoparticles for Biomedical Applications: A Perspective on Synthesis, Drugs, Antimicrobial Activity, and Toxicity. *Antibiotics* **2018**, *7*, 46. [[CrossRef](#)] [[PubMed](#)]
36. Dillert, R.; Taffa, D.H.; Wark, M.; Bredow, T.; Bahnemann, D.W. Research Update: Photoelectrochemical water splitting and photocatalytic hydrogen production using ferrites (MFe<sub>2</sub>O<sub>4</sub>) under visible light irradiation. *APL Mater.* **2015**, *3*, 104001. [[CrossRef](#)]
37. Casbeer, E.; Sharma, V.K.; Li, X.-Z. Synthesis and photocatalytic activity of ferrites under visible light: A review. *Sep. Purif. Technol.* **2012**, *87*, 1–14. [[CrossRef](#)]
38. Buchanan, R.C. (Ed.) *Ceramic Materials for Electronics*, 3rd ed.; Dekker: New York, NY, USA; Basel, Switzerland, 2004; revised expanded; ISBN 9780824740283.
39. Tokubuchi, T.; Arbi, R.I.; Zhenhua, P.; Katayama, K.; Turak, A.; Sohn, W.Y. Enhanced photoelectrochemical water splitting efficiency of hematite (α-Fe<sub>2</sub>O<sub>3</sub>)-Based photoelectrode by the introduction of maghemite (γ-Fe<sub>2</sub>O<sub>3</sub>) nanoparticles. *J. Photochem. Photobiol. A Chem.* **2021**, *410*, 113179. [[CrossRef](#)]
40. Kefeni, K.K.; Mamba, B.B. Photocatalytic application of spinel ferrite nanoparticles and nanocomposites in wastewater treatment: Review. *Sustain. Mater. Technol.* **2020**, *23*, e00140. [[CrossRef](#)]
41. Kushwaha, P.; Chauhan, P. Synthesis of spherical and Rod-Like EDTA assisted α-Fe<sub>2</sub>O<sub>3</sub> nanoparticles via Co-precipitation method. *Mater. Today Proc.* **2021**, *44*, 3086–3090. [[CrossRef](#)]
42. Uma, K.; KrishnaKumar, B.; Pan, G.-T.; Yang, T.C.-K.; Lin, J.-H. Enriched silver plasmon resonance activity on the sonochemical synthesis of ZnO flowers with α-Fe<sub>2</sub>O<sub>3</sub> as an efficient catalyst for photo-Fenton reaction and photo-oxidation of ethanol. *J. Water Process Eng.* **2020**, *34*, 101089. [[CrossRef](#)]
43. Li, Y.; Huang, Y.; Zheng, Y.; Huang, R.; Yao, J. Facile and efficient synthesis of α-Fe<sub>2</sub>O<sub>3</sub> nanocrystals by glucose-assisted thermal decomposition method and its application in lithium ion batteries. *J. Power Sour.* **2019**, *416*, 62–71. [[CrossRef](#)]
44. Tadic, M.; Panjan, M.; Tadic, B.V.; Lazovic, J.; Damnjanovic, V.; Kopani, M.; Kopanja, L. Magnetic properties of hematite (α-Fe<sub>2</sub>O<sub>3</sub>) nanoparticles synthesized by sol-gel synthesis method: The influence of particle size and particle size distribution. *J. Electr. Eng.* **2019**, *70*, 71–76. [[CrossRef](#)]
45. Luo, S.-H.; Hu, D.-B.; Liu, H.; Li, J.-Z.; Yi, T.-F. Hydrothermal synthesis and characterization of α-Fe<sub>2</sub>O<sub>3</sub>/C using acid-pickled iron oxide red for Li-ion batteries. *J. Hazard. Mater.* **2019**, *368*, 714–721. [[CrossRef](#)] [[PubMed](#)]

46. Bozkurt, G. Synthesis and Characterization of  $\alpha$ -Fe<sub>2</sub>O<sub>3</sub> Nanoparticles by Microemulsion Method. *Erzincan Üniv. Fen Bilim. Enst. Derg.* **2020**, *13*, 890–897. [[CrossRef](#)]
47. He, H.-Y. Photocatalytic degradations of dyes on magnetically separable Ni<sub>1-x</sub>Co<sub>x</sub>Fe<sub>2</sub>O<sub>4</sub> nanoparticles synthesized by a hydrothermal process. *Part. Sci. Technol.* **2016**, *34*, 143–151. [[CrossRef](#)]
48. Parsons, J.G.; Lopez, M.L.; Peralta-Videa, J.R.; Gardea-Torresdey, J.L. Determination of arsenic (III) and arsenic (V) binding to microwave assisted hydrothermal synthetically prepared Fe<sub>3</sub>O<sub>4</sub>, Mn<sub>3</sub>O<sub>4</sub>, and MnFe<sub>2</sub>O<sub>4</sub> nanoadsorbents. *Microchem. J.* **2009**, *91*, 100–106. [[CrossRef](#)]
49. Kaur, N.; Kaur, M. Comparative studies on impact of synthesis methods on structural and magnetic properties of magnesium ferrite nanoparticles. *Process. Appl. Ceram.* **2014**, *8*, 137–143. [[CrossRef](#)]
50. Routray, K.L.; Saha, S.; Behera, D. Green synthesis approach for nano sized CoFe<sub>2</sub>O<sub>4</sub> through aloe vera mediated sol-gel auto combustion method for high frequency devices. *Mater. Chem. Phys.* **2019**, *224*, 29–35. [[CrossRef](#)]
51. Zhang, D.; Pu, X.; Du, K.; Yu, Y.M.; Shim, J.J.; Cai, P.; Kim, S.I.; Seo, H.J. Combustion synthesis of magnetic Ag/NiFe<sub>2</sub>O<sub>4</sub> composites with enhanced visible-light photocatalytic properties. *Sep. Purif. Technol.* **2014**, *137*, 82–85. [[CrossRef](#)]
52. Johnson, B.F.G. Nanoparticles in Catalysis. *Top. Catal.* **2003**, *24*, 147–159. [[CrossRef](#)]
53. Govan, J.; Gun'Ko, Y.K. Recent Advances in the Application of Magnetic Nanoparticles as a Support for Homogeneous Catalysts. *Nanomaterials* **2014**, *4*, 222–241. [[CrossRef](#)]
54. Demirelli, M.; Karaoglu, E.; Baykal, A.; Sozeri, H. M-hexaferrite–APTES/Pd(0) Magnetically Recyclable Nano Catalysts (MRCs). *J. Inorg. Organomet. Polym. Mater.* **2013**, *23*, 1274–1281. [[CrossRef](#)]
55. Demirelli, M.; Karaoglu, E.; Baykal, A.; Sozeri, H.; Uysal, E.; Duygulu, O. Recyclable NiFe<sub>2</sub>O<sub>4</sub>–APTES/Pd Magnetic Nanocatalyst. *J. Inorg. Organomet. Polym. Mater.* **2013**, *23*, 937–943. [[CrossRef](#)]
56. Gawande, M.B.; Branco, P.S.; Nogueira, I.D.; Ghumman, C.A.A.; Bundaleski, N.; Santos, A.; Teodoro, O.M.N.D.; Luque, R. Catalytic applications of a versatile magnetically separable Fe–Mo (Nanocat–Fe–Mo) nanocatalyst. *Green Chem.* **2013**, *15*, 682–689. [[CrossRef](#)]
57. Gawande, M.B.; Rath, A.K.; Branco, P.S.; Nogueira, I.D.; Velhinho, A.; Shrikhande, J.J.; Indulkar, U.U.; Jayaram, R.V.; Ghumman, C.A.A.; Bundaleski, N.; et al. Regio- and Chemoselective Reduction of Nitroarenes and Carbonyl Compounds over Recyclable Magnetic Ferrite-Nickel Nanoparticles (Fe<sub>3</sub>O<sub>4</sub>-Ni) by Using Glycerol as a Hydrogen Source. *Chem. Eur. J.* **2012**, *18*, 12628–12632. [[CrossRef](#)] [[PubMed](#)]
58. Gawande, M.B.; Velhinho, A.; Nogueira, I.D.; Ghumman, C.A.A.; Teodoro, O.M.N.D.; Branco, P.S. A facile synthesis of cysteine-ferrite magnetic nanoparticles for application in multicomponent reactions—A sustainable protocol. *RSC Adv.* **2012**, *2*, 6144–6149. [[CrossRef](#)]
59. Gawande, M.B.; Rath, A.; Nogueira, I.D.; Ghumman, C.A.A.; Bundaleski, N.; Teodoro, O.M.N.D.; Branco, P.S. A Recyclable Ferrite-Co Magnetic Nanocatalyst for the Oxidation of Alcohols to Carbonyl Compounds. *Chempluschem* **2012**, *77*, 865–871. [[CrossRef](#)]
60. Duan, H.-Z.; Zhou, F.-L.; Cheng, X.; Chen, G.-H.; Li, Q.-L. Preparation of hollow microspheres of Ce<sub>3+</sub> doped NiCo ferrite with high microwave absorbing performance. *J. Magn. Magn. Mater.* **2017**, *424*, 467–471. [[CrossRef](#)]
61. Gan, L.; Shang, S.; Yuen, C.W.M.; Jiang, S.-X.; Hu, E. Hydrothermal synthesis of magnetic CoFe<sub>2</sub>O<sub>4</sub>/graphene nanocomposites with improved photocatalytic activity. *Appl. Surf. Sci.* **2015**, *351*, 140–147. [[CrossRef](#)]
62. Rehman, M.A.; Yusoff, I.; Alias, Y. Structural, morphological and magnetic investigations of CuCe<sub>0.2</sub>Fe<sub>1.8</sub>O<sub>4</sub> graphene-supported nanocomposites. *Ceram. Int.* **2016**, *42*, 1399–1407. [[CrossRef](#)]
63. Wang, B.; Si, L.; Geng, J.; Su, Y.; Li, Y.; Yan, X.; Chen, L. Controllable magnetic 3D nitrogen-doped graphene gel: Synthesis, characterization, and catalytic performance. *Appl. Catal. B Environ.* **2017**, *204*, 316–323. [[CrossRef](#)]
64. Randhawa, B.S.; Dosanjh, H.S.; Kaur, M. Preparation of Ferrites from the Combustion of Metal Nitrate-Oxalyl Dihydrazide Solutions. *IJEMS* **2005**, *12*, 151–154.
65. Li, X.; Hou, Y.; Zhao, Q.; Wang, L. A general, one-step and template-free synthesis of sphere-like zinc ferrite nanostructures with enhanced photocatalytic activity for dye degradation. *J. Colloid Interface Sci.* **2011**, *358*, 102–108. [[CrossRef](#)]
66. Dom, R.; Subasri, R.; Radha, K.; Borse, P.H. Synthesis of solar active nanocrystalline ferrite, MFe<sub>2</sub>O<sub>4</sub> (M: Ca, Zn, Mg) photocatalyst by microwave irradiation. *Solid State Commun.* **2011**, *151*, 470–473. [[CrossRef](#)]
67. Borhan, A.I.; Samoila, P.; Hulea, V.; Iordan, A.R.; Palamaru, M.N. Photocatalytic activity of spinel ZnFe<sub>2-x</sub>Cr<sub>x</sub>O<sub>4</sub> nanoparticles on removal Orange I azo dye from aqueous solution. *J. Taiwan Inst. Chem. Eng.* **2014**, *45*, 1655–1660. [[CrossRef](#)]
68. Borhan, A.I.; Samoila, P.; Hulea, V.; Iordan, A.R.; Palamaru, M.N. Effect of Al<sup>3+</sup> substituted zinc ferrite on photocatalytic degradation of Orange I azo dye. *J. Photochem. Photobiol. A Chem.* **2014**, *279*, 17–23. [[CrossRef](#)]
69. Jesudoss, S.K.; Vijaya, J.J.; Kennedy, L.J.; Rajan, P.I.; Al-Lohedan, H.A.; Ramalingam, R.J.; Kaviyarasu, K.; Bououdina, M. Studies on the efficient dual performance of Mn<sub>1-x</sub>Ni<sub>x</sub>Fe<sub>2</sub>O<sub>4</sub> spinel nanoparticles in photodegradation and antibacterial activity. *J. Photochem. Photobiol. B Biol.* **2016**, *165*, 121–132. [[CrossRef](#)]
70. Zhang, Z.; Wang, W. Solution combustion synthesis of CaFe<sub>2</sub>O<sub>4</sub> nanocrystal as a magnetically separable photocatalyst. *Mater. Lett.* **2014**, *133*, 212–215. [[CrossRef](#)]
71. Shahid, M.; Jingling, L.; Ali, Z.; Shakir, I.; Warsi, M.F.; Parveen, R.; Nadeem, M. Photocatalytic degradation of methylene blue on magnetically separable MgFe<sub>2</sub>O<sub>4</sub> under visible light irradiation. *Mater. Chem. Phys.* **2013**, *139*, 566–571. [[CrossRef](#)]

72. Zhu, Z.; Li, X.; Zhao, Q.; Li, Y.; Sun, C.; Cao, Y. Photocatalytic performances and activities of Ag-doped CuFe<sub>2</sub>O<sub>4</sub> nanoparticles. *Mater. Res. Bull.* **2013**, *48*, 2927–2932. [CrossRef]
73. Shetty, K.; Renuka, L.; Nagaswarupa, H.P.; Nagabhushana, H.; Anantharaju, K.S.; Rangappa, D.; Prashantha, S.C.; Ashwini, K. A comparative study on CuFe<sub>2</sub>O<sub>4</sub>, ZnFe<sub>2</sub>O<sub>4</sub> and NiFe<sub>2</sub>O<sub>4</sub>: Morphology, Impedance and Photocatalytic studies. *Mater. Today Proc.* **2017**, *4*, 11806–11815. [CrossRef]
74. Lassoued, A.; Lassoued, M.S.; Dkhil, B.; Ammar, S.; Gadri, A. RETRACTED ARTICLE: Photocatalytic degradation of methyl orange dye by NiFe<sub>2</sub>O<sub>4</sub> nanoparticles under visible irradiation: Effect of varying the synthesis temperature. *J. Mater. Sci. Mater. Electron.* **2018**, *29*, 7057–7067. [CrossRef]
75. Roonasi, P.; Mazinani, M. Synthesis and application of barium ferrite/activated carbon composite as an effective solar photocatalyst for discoloration of organic dye contaminants in wastewater. *J. Environ. Chem. Eng.* **2017**, *5*, 3822–3827. [CrossRef]
76. Talebi, R. Preparation and characterization of cobalt ferrite nanoparticles with different capping agents and its photocatalyst application. *J. Mater. Sci. Mater. Electron.* **2017**, *28*, 9749–9754. [CrossRef]
77. Talukdar, S.; Mandal, D.; Mandal, K. Surface modification of Cobalt ferrite nano-hollowspheres for inherent multiple photoluminescence and enhanced photocatalytic activities. *Chem. Phys. Lett.* **2017**, *672*, 57–62. [CrossRef]
78. Parhizkar, J.; Habibi, M.H.; Mosavian, S.Y. Synthesis and Characterization of Nano CoFe<sub>2</sub>O<sub>4</sub> Prepared by Sol-Gel Auto-Combustion with Ultrasonic Irradiation and Evaluation of Photocatalytic Removal and Degradation Kinetic of Reactive Red 195. *Silicon* **2019**, *11*, 1119–1129. [CrossRef]
79. Fang, M.-M.; Shao, J.-X.; Huang, X.-G.; Wang, J.-Y.; Chen, W. Direct Z-scheme CdFe<sub>2</sub>O<sub>4</sub>/g-C<sub>3</sub>N<sub>4</sub> hybrid photocatalysts for highly efficient ceftiofur sodium photodegradation. *J. Mater. Sci. Technol.* **2020**, *56*, 133–142. [CrossRef]
80. Bo, L.; Hu, Y.; Zhang, Z.; Tong, J. Efficient photocatalytic degradation of Rhodamine B catalyzed by SrFe<sub>2</sub>O<sub>4</sub>/g-C<sub>3</sub>N<sub>4</sub> composite under visible light. *Polyhedron* **2019**, *168*, 94–100. [CrossRef]
81. Shakir, I.; Sarfraz, M.; Ali, Z.; Aboud, M.F.A.; Agboola, P.O. Magnetically separable and recyclable graphene-MgFe<sub>2</sub>O<sub>4</sub> nanocomposites for enhanced photocatalytic applications. *J. Alloys Compd.* **2016**, *660*, 450–455. [CrossRef]
82. Grewal, J.K.; Kaur, M.; Sharma, R.K.; Oliveira, A.C.; Garg, V.K.; Sharma, V.K. Structural and Photocatalytic Studies on Oxygen Hyperstoichiometric Titanium-Substituted Strontium Ferrite Nanoparticles. *Magnetochemistry* **2022**, *8*, 120. [CrossRef]
83. Ubhi, M.K.; Kaur, M.; Singh, D.; Javed, M.; Oliveira, A.C.; Garg, V.K.; Sharma, V.K. Hierarchical Nanoflowers of MgFe<sub>2</sub>O<sub>4</sub>, Bentonite and B,P- Co-Doped Graphene Oxide as Adsorbent and Photocatalyst: Optimization of Parameters by Box–Behnken Methodology. *Int. J. Mol. Sci.* **2022**, *23*, 9678. [CrossRef]
84. Singh, E.; Kaur, M.; Sharma, S. Structural tuning of CTAB@MgFe<sub>2</sub>O<sub>4</sub> nanocomposite as peroxidase mimic for H<sub>2</sub>O<sub>2</sub> and glucose sensing. *Mater. Chem. Phys.* **2021**, *271*, 124851. [CrossRef]
85. Kaur, M.; Kaur, M.; Singh, D.; Oliveira, A.C.; Garg, V.K.; Sharma, V.K. Synthesis of CaFe<sub>2</sub>O<sub>4</sub>-NGO Nanocomposite for Effective Removal of Heavy Metal Ion and Photocatalytic Degradation of Organic Pollutants. *Nanomaterials* **2021**, *11*, 1471. [CrossRef] [PubMed]
86. Kaur, M.; Ubhi, M.K.; Grewal, J.K.; Singh, D. Insight into the structural, optical, adsorptive, and photocatalytic properties of MgFe<sub>2</sub>O<sub>4</sub>-bentonite nanocomposites. *J. Phys. Chem. Solids* **2021**, *154*, 110060. [CrossRef]
87. Khushboo; Kaur, M.; Jeet, K. Mechanistic insight into adsorption and photocatalytic potential of magnesium ferrite-bentonite nanocomposite. *J. Photochem. Photobiol. A Chem.* **2022**, *425*, 113717. [CrossRef]
88. Ubhi, M.K.; Kaur, M.; Grewal, J.K.; Oliveira, A.C.; Garg, V.K.; Sharma, V.K. Insight into photocatalytic behavior of magnesium ferrite-bentonite nanocomposite for the degradation of organic contaminants. *J. Mater. Res.* **2022**, *38*, 990–1006. [CrossRef]
89. Guan, X.; Kuang, J.; Yang, L.; Lu, M.; Wang, G. Membrane-Solvothermal Synthesis of Cobalt Ferrite/Reduced Graphene Oxide Nanocomposites and Their Photocatalytic and Electromagnetic Wave Absorption Properties. *ChemistrySelect* **2019**, *4*, 9516–9522. [CrossRef]
90. Sheshmani, S.; Falahat, B.; Nikmaram, F.R. Preparation of magnetic graphene oxide-ferrite nanocomposites for oxidative decomposition of Remazol Black B. *Int. J. Biol. Macromol.* **2017**, *97*, 671–678. [CrossRef]
91. Yoo, P.S.; Reddy, D.A.; Jia, Y.; Bae, S.E.; Huh, S.; Liu, C. Magnetic core-shell ZnFe<sub>2</sub>O<sub>4</sub>/ZnS nanocomposites for photocatalytic application under visible light. *J. Colloid Interface Sci.* **2017**, *486*, 136–143. [CrossRef]
92. Middea, A.; Spinelli, L.S.; Jr, F.G.S.; Neumann, R.; Fernandes, T.L.A.P.; Gomes, O.D.F.M. Preparation and characterization of an organo-palygorskite-Fe<sub>3</sub>O<sub>4</sub> nanomaterial for removal of anionic dyes from wastewater. *Appl. Clay Sci.* **2017**, *139*, 45–53. [CrossRef]
93. Song, W.; Gao, B.; Xu, X.; Xing, L.; Han, S.; Duan, P.; Song, W.; Jia, R. Adsorption-desorption behavior of magnetic amine/Fe<sub>3</sub>O<sub>4</sub> functionalized biopolymer resin towards anionic dyes from wastewater. *Bioresour. Technol.* **2016**, *210*, 123–130. [CrossRef]
94. Soltani, T.; Entezari, M.H. Photolysis and photocatalysis of methylene blue by ferrite bismuth nanoparticles under sunlight irradiation. *J. Mol. Catal. A Chem.* **2013**, *377*, 197–203. [CrossRef]
95. Bian, Z.; Huo, Y.; Zhang, Y.; Zhu, J.; Lu, Y.; Li, H. Aerosol-spray assisted assembly of Bi<sub>2</sub>Ti<sub>2</sub>O<sub>7</sub> crystals in uniform porous microspheres with enhanced photocatalytic activity. *Appl. Catal. B Environ.* **2009**, *91*, 247–253. [CrossRef]
96. Harraz, F.A.; Mohamed, R.M.; Rashad, M.M.; Wang, Y.C.; Sigmund, W. Magnetic nanocomposite based on titania-silica/cobalt ferrite for photocatalytic degradation of methylene blue dye. *Ceram. Int.* **2014**, *40*, 375–384. [CrossRef]
97. Shih, Y.-J.; Su, C.-C.; Chen, C.-W.; Dong, C.-D. Synthesis of magnetically recoverable ferrite (MFe<sub>2</sub>O<sub>4</sub>, M Co, Ni and Fe)-supported TiO<sub>2</sub> photocatalysts for decolorization of methylene blue. *Catal. Commun.* **2015**, *72*, 127–132. [CrossRef]

98. Nardea, S.; Gadegoneb, S.; Lanjewar, M.R.; Lanjewar, R.B. Degradation of Azo Dye Congo Red Using  $\text{Ni}_{0.6}\text{Co}_{0.4}\text{Fe}_2\text{O}_4$  as Photocatalyst. *Pharma Chem.* **2017**, *9*, 115–120.
99. Ge, M.; Liu, W.; Hu, X.-R.; Li, Z.-L. Magnetically separable Ag/AgBr/ $\text{NiFe}_2\text{O}_4$  composite as a highly efficient visible light plasmonic photocatalyst. *J. Phys. Chem. Solids* **2017**, *109*, 1–8. [[CrossRef](#)]
100. Abdel Maksoud, M.I.A.; El-Sayyad, G.S.; El-Khawaga, A.M.; Abd Elkodous, M.; Abokhadra, A.; Elsayed, M.A.; Gobara, M.; Soliman, L.I.; El-Bahnasawy, H.H.; Ashour, A.H. Nanostructured Mg substituted Mn-Zn ferrites: A magnetic recyclable catalyst for outstanding photocatalytic and antimicrobial potentials. *J. Hazard. Mater.* **2020**, *399*, 123000. [[CrossRef](#)]
101. Singh, S.; Kaur, P.; Bansal, S.; Singhal, S. Enhanced photocatalytic performance of Ru-doped spinel nanoferrites for treating recalcitrant organic pollutants in wastewater. *J. Sol-Gel Sci. Technol.* **2019**, *92*, 760–774. [[CrossRef](#)]
102. Tabasum, A.; Alghuthaymi, M.; Qazi, U.Y.; Shahid, I.; Abbas, Q.; Javaid, R.; Nadeem, N.; Zahid, M. UV-Accelerated Photocatalytic Degradation of Pesticide over Magnetite and Cobalt Ferrite Decorated Graphene Oxide Composite. *Plants* **2020**, *10*, 6. [[CrossRef](#)] [[PubMed](#)]
103. Naghizadeh, M.; Taher, M.A.; Tamaddon, A.-M. Facile synthesis and characterization of magnetic nanocomposite ZnO/CoFe<sub>2</sub>O<sub>4</sub> hetero-structure for rapid photocatalytic degradation of imidacloprid. *Heliyon* **2019**, *5*, e02870. [[CrossRef](#)]
104. Wang, M.; Fang, G.; Liu, P.; Zhou, D.; Ma, C.; Zhang, D.; Zhan, J.  $\text{Fe}_3\text{O}_4$ @ $\beta$ -CD nanocomposite as heterogeneous Fenton-like catalyst for enhanced degradation of 4-chlorophenol (4-CP). *Appl. Catal. B Environ.* **2016**, *188*, 113–122. [[CrossRef](#)]
105. Boruah, P.K.; Sharma, B.; Karbhal, I.; Shelke, M.V.; Das, M.R. Ammonia-modified graphene sheets decorated with magnetic  $\text{Fe}_3\text{O}_4$  nanoparticles for the photocatalytic and photo-Fenton degradation of phenolic compounds under sunlight irradiation. *J. Hazard. Mater.* **2016**, *325*, 90–100. [[CrossRef](#)] [[PubMed](#)]
106. Hou, Y.; Li, X.; Zhao, Q.; Chen, G.  $\text{ZnFe}_2\text{O}_4$  multi-porous microbricks/graphene hybrid photocatalyst: Facile synthesis, improved activity and photocatalytic mechanism. *Appl. Catal. B Environ.* **2013**, *142–143*, 80–88. [[CrossRef](#)]
107. Yang, J.; Chen, H.; Gao, J.; Yan, T.; Zhou, F.; Cui, S.; Bi, W. Synthesis of  $\text{Fe}_3\text{O}_4$ /g- $\text{C}_3\text{N}_4$  nanocomposites and their application in the photodegradation of 2,4,6-trichlorophenol under visible light. *Mater. Lett.* **2016**, *164*, 183–189. [[CrossRef](#)]
108. Stoia, M.; Muntean, C.; Militaru, B.  $\text{MnFe}_2\text{O}_4$  nanoparticles as new catalyst for oxidative degradation of phenol by peroxydisulfate. *J. Environ. Sci.* **2017**, *53*, 269–277. [[CrossRef](#)]
109. Arifin, N.; Karim, K.M.R.; Abdullah, H.; Khan, M.R. Synthesis of Titania Doped Copper Ferrite Photocatalyst and Its Photoactivity towards Methylene Blue Degradation under Visible Light Irradiation. *Bull. Chem. React. Eng. Catal.* **2019**, *14*, 219–227. [[CrossRef](#)]
110. Mapossa, A.B.; Mhike, W.; Adalima, J.L.; Tichapondwa, S. Removal of Organic Dyes from Water and Wastewater Using Magnetic Ferrite-Based Titanium Oxide and Zinc Oxide Nanocomposites: A Review. *Catalysts* **2021**, *11*, 1543. [[CrossRef](#)]
111. Gupta, N.K.; Ghaffari, Y.; Kim, S.; Bae, J.; Kim, K.S.; Saifuddin, M. Photocatalytic Degradation of Organic Pollutants over  $\text{MFe}_2\text{O}_4$  (M = Co, Ni, Cu, Zn) Nanoparticles at Neutral PH. *Sci. Rep.* **2020**, *10*, 4942. [[CrossRef](#)]
112. Makofane, A.; Motaung, D.E.; Hintsho-Mbita, N.C. Photocatalytic degradation of methylene blue and sulfisoxazole from water using biosynthesized zinc ferrite nanoparticles. *Ceram. Int.* **2021**, *47*, 22615–22626. [[CrossRef](#)]
113. Rashmi, S.K.; Bhojya Naik, H.S.; Jayadevappa, H.; Viswanath, R.; Patil, S.B.; Madhukara Naik, M. Solar light responsive Sm-Zn ferrite nanoparticle as efficient photocatalyst. *Mater. Sci. Eng. B* **2017**, *225*, 86–97. [[CrossRef](#)]
114. Kirankumar, V.S.; Sumathi, S. Copper and cerium co-doped cobalt ferrite nanoparticles: Structural, morphological, optical, magnetic, and photocatalytic properties. *Environ. Sci. Pollut. Res.* **2019**, *26*, 19189–19206. [[CrossRef](#)]
115. Mahdikhah, V.; Saadatkia, S.; Sheibani, S.; Ataie, A. Outstanding photocatalytic activity of  $\text{CoFe}_2\text{O}_4$ /rGO nanocomposite in degradation of organic dyes. *Opt. Mater.* **2020**, *108*, 110193. [[CrossRef](#)]
116. Manikandan, A.; Hema, E.; Durka, M.; Seevakan, K.; Alagesan, T.; Arul Antony, S. Room Temperature Ferromagnetism of Magnetically Recyclable Photocatalyst of  $\text{Cu}_{1-x}\text{Mn}_x\text{Fe}_2\text{O}_4\text{-TiO}_2$  ( $0.0 \leq x \leq 0.5$ ) Nanocomposites. *J. Supercond. Nov. Magn.* **2015**, *28*, 1783–1795. [[CrossRef](#)]
117. Grewal, J.K.; Kaur, M.; Ubhi, M.K.; Oliveira, A.C.; Garg, V.K.; Sharma, V.K. Structural, magnetic, and photocatalytic properties of core-shell reversal nanocomposites of titanium-doped strontium ferrite and silica. *J. Mater. Res.* **2023**, *38*, 1019–1034. [[CrossRef](#)]
118. Mohan, H.; Ramalingam, V.; Adithan, A.; Natesan, K.; Seralathan, K.-K.; Shin, T. Highly efficient visible light driven photocatalytic activity of zinc/ferrite: Carbamazepine degradation, mechanism and toxicity assessment. *J. Hazard. Mater.* **2021**, *416*, 126209. [[CrossRef](#)] [[PubMed](#)]
119. Nguyen, T.B.; Huang, C.P.; Doong, R.-A. Photocatalytic degradation of bisphenol A over a  $\text{ZnFe}_2\text{O}_4/\text{TiO}_2$  nanocomposite under visible light. *Sci. Total Environ.* **2019**, *646*, 745–756. [[CrossRef](#)]
120. Nguyen, L.T.T.; Nguyen, L.T.H.; Manh, N.C.; Quoc, D.N.; Quang, H.N.; Nguyen, H.T.T.; Nguyen, D.C.; Bach, L.G. A Facile Synthesis, Characterization, and Photocatalytic Activity of Magnesium Ferrite Nanoparticles via the Solution Combustion Method. *J. Chem.* **2019**, *2019*, 3428681. [[CrossRef](#)]
121. Sun, M.; Han, X.; Chen, S. Synthesis and photocatalytic activity of nano-cobalt ferrite catalyst for the photo-degradation various dyes under simulated sunlight irradiation. *Mater. Sci. Semicond. Process.* **2019**, *91*, 367–376. [[CrossRef](#)]
122. Sundararajan, M.; John Kennedy, L.; Nithya, P.; Judith Vijaya, J.; Bououdina, M. Visible Light Driven Photocatalytic Degradation of Rhodamine B Using Mg Doped Cobalt Ferrite Spinel Nanoparticles Synthesized by Microwave Combustion Method. *J. Phys. Chem. Solids* **2017**, *108*, 61–75. [[CrossRef](#)]
123. Singh, G.; Kaur, M.; Garg, V.K.; Oliveira, A.C. Oxygen hyper stoichiometric trimetallic titanium doped magnesium ferrite: Structural and photocatalytic studies. *Ceram. Int.* **2022**, *48*, 24476–24484. [[CrossRef](#)]

124. Sharma, R.; Komal; Kumar, V.; Bansal, S.; Singhal, S. Boosting the catalytic performance of pristine  $\text{CoFe}_2\text{O}_4$  with yttrium ( $\text{Y}^{3+}$ ) inclusion in the spinel structure. *Mater. Res. Bull.* **2017**, *90*, 94–103. [[CrossRef](#)]
125. Dhiman, M.; Chudasama, B.; Kumar, V.; Tikoo, K.B.; Singhal, S. Augmenting the photocatalytic performance of cobalt ferrite via change in structural and optical properties with the introduction of different rare earth metal ions. *Ceram. Int.* **2019**, *45*, 3698–3709. [[CrossRef](#)]
126. Sathishkumar, P.; Mangalaraja, R.V.; Anandan, S.; Ashokkumar, M.  $\text{CoFe}_2\text{O}_4/\text{TiO}_2$  nanocatalysts for the photocatalytic degradation of Reactive Red 120 in aqueous solutions in the presence and absence of electron acceptors. *Chem. Eng. J.* **2013**, *220*, 302–310. [[CrossRef](#)]
127. Barakat, N.A.M.; Kanjwal, M.A.; Chronakis, I.S.; Kim, H.Y. Influence of temperature on the photodegradation process using Ag-doped  $\text{TiO}_2$  nanostructures: Negative impact with the nanofibers. *J. Mol. Catal. A Chem.* **2013**, *366*, 333–340. [[CrossRef](#)]
128. Kumar, G.P.A. A Review on the Factors Affecting the Photocatalytic Degradation of Hazardous Materials. *Mater. Sci. Eng. Int. J.* **2017**, *1*, 1–10. [[CrossRef](#)]
129. Ubhi, M.K.; Kaur, M.; Singh, D.; Sharma, V.K. Structural and adsorptive properties of boron- and phosphorous-doped graphene oxide: Insight into effective removal of Pb (II) and as (III). *J. Water Process Eng.* **2023**, *52*, 103539. [[CrossRef](#)]
130. Zhao, Y.; Lin, C.; Bi, H.; Liu, Y.; Yan, Q. Magnetically separable  $\text{CuFe}_2\text{O}_4/\text{AgBr}$  composite photocatalysts: Preparation, characterization, photocatalytic activity and photocatalytic mechanism under visible light. *Appl. Surf. Sci.* **2017**, *392*, 701–707. [[CrossRef](#)]
131. Koe, W.S.; Lee, J.W.; Chong, W.C.; Pang, Y.L.; Sim, L.C. An overview of photocatalytic degradation: Photocatalysts, mechanisms, and development of photocatalytic membrane. *Environ. Sci. Pollut. Res.* **2020**, *27*, 2522–2565. [[CrossRef](#)]
132. Zafar, M.N.; Dar, Q.; Nawaz, F.; Zafar, M.N.; Iqbal, M.; Nazar, M.F. Effective adsorptive removal of azo dyes over spherical ZnO nanoparticles. *J. Mater. Res. Technol.* **2019**, *8*, 713–725. [[CrossRef](#)]
133. Gomes, J.; Lincho, J.; Domingues, E.; Quinta-Ferreira, R.M.; Martins, R.C. N-TiO<sub>2</sub> Photocatalysts: A Review of Their Characteristics and Capacity for Emerging Contaminants Removal. *Water* **2019**, *11*, 373. [[CrossRef](#)]
134. Pasinszki, T.; Krebsz, M. Synthesis and Application of Zero-Valent Iron Nanoparticles in Water Treatment, Environmental Remediation, Catalysis, and Their Biological Effects. *Nanomaterials* **2020**, *10*, 917. [[CrossRef](#)]
135. Miri, A.; Mahabbati, F.; Najafidoust, A.; Miri, M.J.; Sarani, M. Nickel oxide nanoparticles: Biosynthesized, characterization and photocatalytic application in degradation of methylene blue dye. *Inorg. Nano-Metal Chem.* **2022**, *52*, 122–131. [[CrossRef](#)]
136. Raliya, R.; Avery, C.; Chakrabarti, S.; Biswas, P. Photocatalytic degradation of methyl orange dye by pristine titanium dioxide, zinc oxide, and graphene oxide nanostructures and their composites under visible light irradiation. *Appl. Nanosci.* **2017**, *7*, 253–259. [[CrossRef](#)]
137. Singh, S.; Kumar, V.; Romero, R.; Sharma, K.; Singh, J. Applications of Nanoparticles in Wastewater Treatment. In *Nanobiotechnology in Bioformulations*; Prasad, R., Kumar, V., Kumar, M., Choudhary, D., Eds.; Springer International Publishing: Cham, Switzerland, 2019; pp. 395–418. ISBN 9783030170608.
138. Dimapilis, E.A.S.; Hsu, C.-S.; Mendoza, R.M.O.; Lu, M.-C. Zinc oxide nanoparticles for water disinfection. *Sustain. Environ. Res.* **2018**, *28*, 47–56. [[CrossRef](#)]
139. Dobrucka, R. Facile Synthesis of Trimetallic Nanoparticles Au/CuO/ZnO Using *Vitex Agnus-Castus* Extract and Their Activity in Degradation of Organic Dyes. *Int. J. Environ. Anal. Chem.* **2021**, *101*, 2046–2057. [[CrossRef](#)]
140. Kirankumar, V.S.; Sumathi, S. Photocatalytic and antibacterial activity of bismuth and copper co-doped cobalt ferrite nanoparticles. *J. Mater. Sci. Mater. Electron.* **2018**, *29*, 8738–8746. [[CrossRef](#)]
141. Sun, F.; Zeng, Q.; Tian, W.; Zhu, Y.; Jiang, W. Magnetic  $\text{MFe}_2\text{O}_4\text{-Ag}_2\text{O}$  ( $\text{M} = \text{Zn, Co, \& Ni}$ ) composite photocatalysts and their application for dye wastewater treatment. *J. Environ. Chem. Eng.* **2019**, *7*, 103011. [[CrossRef](#)]
142. Babu, B.; Koutavarapu, R.; Shim, J.; Yoo, K.  $\text{SnO}_2$  quantum dots decorated  $\text{NiFe}_2\text{O}_4$  nanoplates: 0D/2D heterojunction for enhanced visible-light-driven photocatalysis. *Mater. Sci. Semicond. Process.* **2020**, *107*, 104834. [[CrossRef](#)]
143. Kuang, M.; Zhang, J.; Wang, W.; Chen, J.; Liu, R.; Xie, S.; Wang, J.; Ji, Z. Synthesis of octahedral-like  $\text{ZnO}/\text{ZnFe}_2\text{O}_4$  heterojunction photocatalysts with superior photocatalytic activity. *Solid State Sci.* **2019**, *96*, 105901. [[CrossRef](#)]
144. Emadian, S.S.; Ghorbani, M.; Bakeri, G. Magnetically separable  $\text{CoFe}_2\text{O}_4/\text{ZrO}_2$  nanocomposite for the photocatalytic reduction of hexavalent chromium under visible light irradiation. *Synth. Met.* **2020**, *267*, 116470. [[CrossRef](#)]
145. Silva, E.D.N.; Brasileiro, I.L.O.; Madeira, V.S.; de Farias, B.A.; Ramalho, M.L.A.; Rodríguez-Aguado, E.; Rodríguez-Castellón, E. Reusable  $\text{CuFe}_2\text{O}_4\text{-Fe}_2\text{O}_3$  catalyst synthesis and application for the heterogeneous photo-Fenton degradation of methylene blue in visible light. *J. Environ. Chem. Eng.* **2020**, *8*, 104132. [[CrossRef](#)]
146. Munir, S.; Rasheed, A.; Zulfikar, S.; Aadil, M.; Agboola, P.O.; Shakir, I.; Warsi, M.F. Synthesis, characterization and photocatalytic parameters investigation of a new  $\text{CuFe}_2\text{O}_4/\text{Bi}_2\text{O}_3$  nanocomposite. *Ceram. Int.* **2020**, *46*, 29182–29190. [[CrossRef](#)]
147. Lu, D.; Zhang, Y.; Lin, S.; Wang, L.; Wang, C. Synthesis of magnetic  $\text{ZnFe}_2\text{O}_4$ /graphene composite and its application in photocatalytic degradation of dyes. *J. Alloys Compd.* **2013**, *579*, 336–342. [[CrossRef](#)]
148. Behera, A.; Mansingh, S.; Das, K.K.; Parida, K. Synergistic  $\text{ZnFe}_2\text{O}_4$ -carbon allotropes nanocomposite photocatalyst for norfloxacin degradation and Cr (VI) reduction. *J. Colloid Interface Sci.* **2019**, *544*, 96–111. [[CrossRef](#)]
149. Sudhaik, A.; Raizada, P.; Shandilya, P.; Singh, P. Magnetically recoverable graphitic carbon nitride and  $\text{NiFe}_2\text{O}_4$  based magnetic photocatalyst for degradation of oxytetracycline antibiotic in simulated wastewater under solar light. *J. Environ. Chem. Eng.* **2018**, *6*, 3874–3883. [[CrossRef](#)]

150. Palanivel, B.; Ayappan, C.; Jayaraman, V.; Chidambaram, S.; Maheswaran, R.; Mani, A. Inverse spinel NiFe<sub>2</sub>O<sub>4</sub> deposited g-C<sub>3</sub>N<sub>4</sub> nanosheet for enhanced visible light photocatalytic activity. *Mater. Sci. Semicond. Process.* **2019**, *100*, 87–97. [[CrossRef](#)]
151. Wang, Q.; Hui, J.; Li, J.; Cai, Y.; Yin, S.; Wang, F.; Su, B. Photodegradation of methyl orange with PANI-modified BiOCl photocatalyst under visible light irradiation. *Appl. Surf. Sci.* **2013**, *283*, 577–583. [[CrossRef](#)]
152. Deng, Y.; Tang, L.; Zeng, G.; Dong, H.; Yan, M.; Wang, J.; Hu, W.; Wang, J.; Zhou, Y.; Tang, J. Enhanced visible light photocatalytic performance of polyaniline modified mesoporous single crystal TiO<sub>2</sub> microsphere. *Appl. Surf. Sci.* **2016**, *387*, 882–893. [[CrossRef](#)]
153. Zhou, J.; Zhang, Z.; Kong, X.; He, F.; Zhao, R.; Wu, R.; Wei, T.; Wang, L.; Feng, J. A novel P-N heterojunction with staggered energy level based on ZnFe<sub>2</sub>O<sub>4</sub> decorating SnS<sub>2</sub> nanosheet for efficient photocatalytic degradation. *Appl. Surf. Sci.* **2020**, *510*, 145442. [[CrossRef](#)]
154. Huang, S.; Xu, Y.; Zhou, T.; Xie, M.; Ma, Y.; Liu, Q.; Jing, L.; Xu, H.; Li, H. Constructing magnetic catalysts with in-situ solid-liquid interfacial photo-Fenton-like reaction over Ag<sub>3</sub>PO<sub>4</sub>@NiFe<sub>2</sub>O<sub>4</sub> composites. *Appl. Catal. B Environ.* **2018**, *225*, 40–50. [[CrossRef](#)]
155. Li, X.; Wang, L.; Zhang, L.; Zhuo, S. A facile route to the synthesis of magnetically separable BiOBr/NiFe<sub>2</sub>O<sub>4</sub> composites with enhanced photocatalytic performance. *Appl. Surf. Sci.* **2017**, *419*, 586–594. [[CrossRef](#)]
156. Eskandari, N.; Nabyouni, G.; Masoumi, S.; Ghanbari, D. Preparation of a new magnetic and photo-catalyst CoFe<sub>2</sub>O<sub>4</sub>-SrTiO<sub>3</sub> perovskite nanocomposite for photo-degradation of toxic dyes under short time visible irradiation. *Compos. Part B Eng.* **2019**, *176*, 107343. [[CrossRef](#)]
157. Jia, J.; Du, X.; Zhang, Q.; Liu, E.; Fan, J. Z-scheme MgFe<sub>2</sub>O<sub>4</sub>/Bi<sub>2</sub>MoO<sub>6</sub> heterojunction photocatalyst with enhanced visible light photocatalytic activity for malachite green removal. *Appl. Surf. Sci.* **2019**, *492*, 527–539. [[CrossRef](#)]
158. Wang, J.; Zhang, Q.; Deng, F.; Luo, X.; Dionysiou, D.D. Rapid toxicity elimination of organic pollutants by the photocatalysis of environment-friendly and magnetically recoverable step-scheme SnFe<sub>2</sub>O<sub>4</sub>/ZnFe<sub>2</sub>O<sub>4</sub> nano-heterojunctions. *Chem. Eng. J.* **2020**, *379*, 122264. [[CrossRef](#)]
159. Suresh, R.; Rajendran, S.; Kumar, P.S.; Vo, D.-V.N.; Cornejo-Ponce, L. Recent advancements of spinel ferrite based binary nanocomposite photocatalysts in wastewater treatment. *Chemosphere* **2021**, *274*, 129734. [[CrossRef](#)] [[PubMed](#)]
160. Mir, S.H.; Jennings, B.D.; Akinoglu, G.E.; Selkirk, A.; Gatensby, R.; Mokarian-Tabari, P. Enhanced Dye Degradation through Multi-Particle Confinement in a Porous Silicon Substrate: A Highly Efficient, Low Band Gap Photocatalyst. *Adv. Opt. Mater.* **2021**, *9*, 2002238. [[CrossRef](#)]
161. Wilson, A.; Mishra, S.R.; Gupta, R.; Ghosh, K. Preparation and photocatalytic properties of hybrid core-shell reusable CoFe<sub>2</sub>O<sub>4</sub>-ZnO nanospheres. *J. Magn. Magn. Mater.* **2012**, *324*, 2597–2601. [[CrossRef](#)]
162. Suwarnkar, M.B.; Dhabbe, R.S.; Kadam, A.N.; Garadkar, K.M. Enhanced photocatalytic activity of Ag doped TiO<sub>2</sub> nanoparticles synthesized by a microwave assisted method. *Ceram. Int.* **2014**, *40*, 5489–5496. [[CrossRef](#)]
163. Zhu, X.; Zhang, F.; Wang, M.; Ding, J.; Sun, S.; Bao, J.; Gao, C. Facile synthesis, structure and visible light photocatalytic activity of recyclable ZnFe<sub>2</sub>O<sub>4</sub>/TiO<sub>2</sub>. *Appl. Surf. Sci.* **2014**, *319*, 83–89. [[CrossRef](#)]
164. Gupta, V.K.; Eren, T.; Atar, N.; Yola, M.L.; Parlak, C.; Karimi-Maleh, H. CoFe<sub>2</sub>O<sub>4</sub>@TiO<sub>2</sub> decorated reduced graphene oxide nanocomposite for photocatalytic degradation of chlorpyrifos. *J. Mol. Liq.* **2015**, *208*, 122–129. [[CrossRef](#)]
165. Masunga, N.; Mmesli, O.K.; Kefeni, K.K.; Mamba, B.B. Recent advances in copper ferrite nanoparticles and nanocomposites synthesis, magnetic properties and application in water treatment: Review. *J. Environ. Chem. Eng.* **2019**, *7*, 103179. [[CrossRef](#)]
166. Rani, M.; Rachna; Shanker, U. Efficient photocatalytic degradation of Bisphenol A by metal ferrites nanoparticles under sunlight. *Environ. Technol. Innov.* **2020**, *19*, 100792. [[CrossRef](#)]

**Disclaimer/Publisher's Note:** The statements, opinions and data contained in all publications are solely those of the individual author(s) and contributor(s) and not of MDPI and/or the editor(s). MDPI and/or the editor(s) disclaim responsibility for any injury to people or property resulting from any ideas, methods, instructions or products referred to in the content.